RESEARCH ARTICLE



WILEY

A Lagrangian meshfree mesoscale simulation of powder bed fusion additive manufacturing of metals

Zongyue $Fan^1 \mid Hao\ Wang^1 \mid Zhida\ Huang^1 \mid Huming\ Liao^2 \mid \ Jiang\ Fan^2 \mid Jian\ Lu^3 \mid Chong\ Liu^3 \mid Bo\ Li^1 \mid$

Correspondence

Bo Li, Department of Mechanical and Aerospace Engineering, Case Western Reserve University, Cleveland, OH 44106, USA.

Email: bxl295@case.edu

Abstract

We present a powder-scale computational framework to predict the microstructure evolution of metals in powder bed fusion additive manufacturing (PBF AM) processes based on the hot optimal transportation meshfree (HOTM) method. The powder bed is modeled as discrete and deformable three-dimensional bodies by integrating statistic information from experiments, including particle size and shape, and powder packing density. Tractions in Lagrangian framework are developed to model the recoil pressure and surface tension. The laser beam is applied to surfaces of particles and substrate dynamically as a heat flux with user-specified beam size, power, scanning speed, and path. The linear momentum and energy conservation equations are formulated in the Lagrangian configuration and solved simultaneously in a monolithic way by the HOTM method to predict the deformation, temperature, contact mechanisms, and fluid-structure interactions in the powder bed. The numerical results are validated against single track experiments. Various powder bed configurations, laser powers, and speed are investigated to understand the influence of dynamic contact and inelastic material behavior on the deformation, heat transfer, and phase transition of the powder bed. The formation of defects in the microstructure of 3D printed metals, including pores, partially, and unmelted particles, is predicted by the proposed computational scheme.

KEYWORDS

defects formation, HOTM method, meshfree methods, powder bed fusion additive manufacturing, powder-scale simulation

1 | INTRODUCTION

Additive manufacturing (AM) technology enables a high degree of design freedoms, manufacture of customized products at reasonable costs, and the development of novel structured high-performance components.¹ The rapidly growing interest in AM across the world has been highlighted by numerous publications and reports.²⁻⁴ Among a variety of AM techniques, powder bed fusion (PBF) based AM technology is one of the most versatile and commercialized advances for metal parts.⁵ In the PBF processes, such as selective laser melting (SLM) and electron-beam melting (EBM), high power energy beams scan a powder bed's surface to melt the powder particles, which then fuse to the previous layers

¹Department of Mechanical and Aerospace Engineering, Case Western Reserve University, Cleveland, Ohio

²School of Energy and Power Engineering, Beihang University, Beijing, China

³Guangdong Institute of Aeronautics and Astronautics Equipment and Technology, Zhuhai, China

as the molten material cools. Nevertheless, it is recognized that metal parts built directly via PBF processes without postprocessing are generally subjected to more defect inclusions. According to the Venn diagram of overlapping process-structure-property-performance relations,⁶ the macroscopic properties and responses of the printed material intimately rely on the underlying microstructure, which is further controlled by the manufacturing processing parameters. Thus, the main research effort in PBF AM technology is to enhance the reliability of the manufacturing processes and the quality of printed metal products by reducing defects in their microstructure, both experimentally and numerically.

Experimental advances on PBF AM process control mainly rely on the trial-and-error method. For instance, Kamath et al⁷ studied the processing parameters for high-quality additive manufactured 316L stainless steel with laser power up to 400 W. In the work of Kempen et al,⁸ preheating temperature is suggested to improve the quality of the final product. Bertoli et al⁹ studied the effect of various laser power and speed on the geometry of the melt pool. Gong et al¹⁰ and Kruth et al¹¹ found that there exists a "processing window" to obtain good product quality. Cunningham et al¹² developed a micro x-ray system for the characterization of porosity in the PBF AM manufactured samples to exam the product quality accurately. Recently, a number of studies of the melt pool thermodynamics are conducted by in-situ measurements using high-speed cameras, disclosing a diversity of details of the PBF process, such as the motion of the powder particles and the formation of the melt pool. ¹³⁻¹⁸ While many efforts are devoted to building the relationship between the processing parameters and the product quality experimentally, Yadroitsev et al¹⁹ indicate that there are more than 130 parameters in the PBF AM process related to the final quality of the product. The determination of the process-structure-property-performance correlation by laboratory testings may quickly become time-consuming and expensive.

An attractive alternative to addressing this challenge is through numerical modeling and predictive simulations. Grid-based numerical methods, such as the finite element method (FEM), ²⁰⁻²² finite volume method (FVM), ²³⁻²⁹ arbitrary Lagrangian-Eulerian method (ALE), ³⁰⁻³² and the lattice Boltzmann method (LBM), ³³⁻³⁶ are popular numerical solutions for modeling metal PBF AM processes. ¹ Most of the simulations consider the powder bed as a continuous media and predict the temperature distribution and residual stresses of the printed material. ^{20,21,25,37-41} Yuan and Gu, ²⁵ for example, performed finite volume simulations of PBF-AM to study the effect of Marangoni convection on heat and mass transfer. Their results show that the thermodynamic flow is symmetric along the melt track and does not exhibit fluctuations due to a randomly packed powder particles. Gusarov et al ³⁹ studied the temperature distribution and shape of the melt pool on a continuous powder bed and suggested a qualitative relation between the melt pool size and laser power. In Cheng et al, ²¹ the powder bed porosity is found to play a critical role in controlling the thermal characteristics and formation of the melt pool from the prediction of FE simulations.

Nevertheless, the powder beds' effective models may not account for the discrete nature of the powder bed and miss fine-scale physics, such as thermodynamics of a discrete system, single-particle dynamic responses, and inter-particle contact, fluid-structure interactions (FSIs), and multiphase flow in a porous media. Interactions between particles primarily affect the thermomechanical behavior of the melt pool and heat transfer in the powder bed. Furthermore, high-fidelity predictions of the formation of topological defects in the microstructure of printed metallic parts, including voids, micro-cracks, unmelted, or partially melted particles, can only be obtained by concerning the powder bed as a collection of discrete particles explicitly. A considerable amount of pioneering work on powder-scale simulations of PBF AM processes has been proposed by researchers with the dynamics at a particle level. Attar and Korner³³ employed the LBM for 2D simulations of the AM process. Gurtler et al²⁸ present the first 3D mesoscopic model for the melting and solidification process in the powder bed by combining the FVM and the volume of fluid (VoF) method, in which single-sized and uniformly arranged powder particles are simulated. Khairallah and Anderson³⁰ developed a 3D mesoscopic model using ALE3D for the study of the powder bed by integrating a particle size distribution measured in experiments. They emphasized the importance of resolving the particle point contacts to capture the correct reduced effective thermal conductivity of the powder, and the role of surface tension in breaking up the melt track into undesirable ball defects at higher laser scanning speeds due to a variant of the Plateau-Rayleigh instability theory. Khairallah et al³¹ further studied the effects of recoil pressure and Marangoni convection on the formation of pores, spatter, and denudation zones. Markl et al³⁶ extended the 3D LBM simulations for various laser scanning strategies. Yan et al^{27,29} reported the effect of multiple laser scanning tracks on the formation of defects during the multiple-layer AM process using the FVM/VoF method. Gu et al⁴² employed a similar approach to quantify the influence of the powder size and the powder paving process on the flow behavior of powder system and the subsequent melt pool formation and solidification characteristics of Inconel 718 composites.

However, the current state-of-the-art powder-scale simulations either consider one single layer of particles physically attached to the substrate or suffer from challenges to accurately model the movement of individual particles and multibody dynamic contact among particles in a multilayer powder bed. Xray experiments of PBF AM processes have shown the speed of ejected particles can reach as high as 7 m/s. ^{13,14} The powder bed is denuded due to the motion of particles

driven by the recoil pressure and dynamic contact forces, as observed in high-speed camera measurements. 18 It has been suggested that solid particle-particle contact and molten material-solid particle interactions play a significant role in the PBF AM processes. 13-18 The effective mechanical and thermal properties of the powder bed, such as heat conductivity, vary drastically as the particle-particle interaction is evolving. The probability of dynamic contact and the contact area change in a powder bed is further determined by the processing parameters, including the powder bed packing density, particle size and shape distribution, recoil pressure, and others. Thus, quantification of the correlation between the processing parameters and the microstructure of printed material necessitates an in-depth understanding of the dynamic contact and deformation mechanism in a powder bed at a particle level. On the other hand, due to the thermal softening of metallic materials, it is not clear whether there may be plastic deformation experienced by the solid metallic particles under recoil pressure and contact forces before fully melted. The influence of plastic deformation of metallic particles on the motion and deformation of the powder bed has not been studied extensively. Current powder-scale simulations of PBF AM processes based on the Eulerian methods suffer from some inherent drawbacks to model free surface and material interfaces, history-dependent material responses, multibody dynamic contact and fracture. Recently, Wang et al⁴³ proposed the hot optimal transportation meshfree (HOTM) method for the high-fidelity prediction of materials dynamic behavior under extreme thermomechanical coupling conditions. The HOTM method is formulated in the incremental updated Lagrangian framework and combines the optimal transportation meshfree (OTM) method⁴⁴ with the variational thermomechanical constitutive updates. 45,46 The variational structure of a dynamic system with general internal dissipative mechanisms, such as plasticity and viscosity, is discretized in time by applying the optimal transportation theory, while material points and nodes are introduced for the spatial discretization of the domain. The fully discretized linear momentum and energy conservation equations are solved simultaneously to predict the deformation, temperature, and internal variables of the domain. As a result of the variational principles, strongly coupled thermo-mechanical FSI problems can be solved monolithically with robustness and efficiency. As a pure Lagrangian meshfree approach, the HOTM method provides a highly suitable solution to simulate problems with free surfaces, dynamic contact, inelastic material responses, and fracture.

In this article, we present a mesoscale computational capability at the particle level based on the HOTM method to study the dynamic contact and deformation mechanism in a multiple layer powder bed. The powder bed is modeled as an aggregation of discrete particles by explicitly accounting for the particle size, shape distribution, and packing density. Each particle is discretized by material points and nodes within the HOTM approach, where a phase-aware material model is assigned to the material points to describe the nonlinear inelastic behavior of the material with rate-sensitivity, temperature-dependence, and phase change. Due to the weak Kronecker-Delta property of the local maximum entropy (LME) meshfree approximation scheme adopted in the HOTM method, the displacement and temperature boundary conditions can be applied directly to the surface nodes as convenient as the FEM. High power energy input is modeled as a heat flux boundary condition applied to free surface nodes, which are automatically tracked without extra computational expenses in the Lagrangian framework. In specific, a super-Gaussian heat flux model is employed for the power beam such that the beam size, power, scanning speed, and path can be readily specified in the simulations. Surface tension and recoil pressure are modeled as temperature-dependent traction boundary conditions. The OTM contact algorithm is employed to simulate the dynamic contact among the solid particles and FSIs. For the fluid phase, the nearly incompressibility condition is considered. Finally, the complex thermomechanical history experienced by individual metallic particles as a high power energy input deposits to their free surfaces can be predicted by solving the conservation equations using the HOTM method. Consequently, the strongly coupled thermomechanical behavior of the powder bed can be illustrated in detail at the mesoscopic scale to predict the melt pool thermodynamics and the formation of the topological defects in the microstructure. The sensitivity of the melt pool dimensions and defects in the printed material, such as voids, partially melted or unmelted particles, on the particle size and thermomechanical properties, powder bed packing density, and processing parameters (e.g., laser power, trajectories, and speed, and more) can be quantified. A fundamental understanding of the influence of dynamic contact and plastic material behavior on the deformation, heat transfer, and phase transition mechanism of the powder bed can be developed.

The outline of this article is as follows: we begin by reconstructing the powder bed geometry for the numerical study based on experimental measurements in Section 2. A brief introduction to the HOTM method is given in Section 3. We summarize the governing equations, variational formulation, and temporal and spatial discretization of the numerical framework. Boundary conditions of the PBF AM process and the dynamic contact algorithm are also discussed in Section 3. We validate the powder-scale simulation of PBF AM processes by comparing the predicted melt pool width and porosity of the printed material to experimental results of Dilip et al⁴⁷ in Section 4. Section 5 shows our numerical study of the effects of the powder bed packing density and thickness on the product quality. The influence of various laser

power and scanning speed on the melt pool dimensions and microstructure characteristics of the printed material is also quantified. Some interesting phenomena we discovered from the simulation results are discussed in conclusion.

2 | NUMERICAL REPRESENTATION OF POWDER BED

For high-fidelity simulations of PBF processes, the numerical representation of a physical powder bed based on experimental statistic information directly determines the thermodynamics of the melt pool and the formation of the printed material's microstructure. Recently, the topic of modeling the powder spreading process has attracted considerable research interest. A subset of the central processing parameters considered in our simulations is the powder particles characteristics and the powder-bed geometry, including the powder particle size and shape distribution, particle quality (such as pores and second phase inclusions), thermomechanical properties, and powder bed packing density.

The geometrical modeling process to create a realistic powder bed is implemented at the following three steps:

- Step 1: Randomly insert a number of particles with a desired size and shape distribution measured from experiments into a bounded box. The height of the box is defined in the normal direction of the powder bed surface, which should be big enough to allow for conveniently inserting the particles, but the length and width of the box are the final dimensions of the computational domain. The separating axis theorem and oriented bounding boxes (OBB) tree are employed⁵⁵ to avoid collision between particles with various three-dimensional shapes. The random insertion can result in a loosely packed powder bed with packing density less than 5%, as shown in Figure 1A.
- Step 2: Compress the loosely packed powder bed to reach the pre-defined packing density using the discrete element method (DEM).⁵⁶ DEM is one of the most popular numerical approaches to model the particle spreading during the PBF process.⁵⁷ In a DEM calculation, the motion of particles is predicted based on the Newtonian mechanics. Contact forces, such as the normal contact and frictional forces, and non-contact forces, such as the von der Waals force, can be considered in the model. In the reconstruction of the powder bed, we assume that the metal particles are undergoing rigid body motion, and only the normal contact force is concerned between two neighboring particles. The normal force becomes very large as two particles collide and turn to be zero sharply once they are separate. In this step, the DEM computation enforces nonpenetration conditions between the particles. The multisphere method is used to generate nonspherical particles,⁵⁸ in which they are approximated by a few spheres overlapping to form a clump, and all the contacts are detected as sphere-sphere interaction. Powders with bad quality, such as hollow spheres and particles with a rough surface or a crack as observed in experiments, can also be generated in this way. We can terminate the DEM calculations while the current packing density satisfies the user-specific requirement, as shown in Figure 1B,C, where the pre-defined packing density is 22% and 55%, respectively. In case that appropriate body forces are applied to the particles, such as gravity, the DEM calculation converges to a physical value measured in experiments as the powder bed finally becomes stable and densely packed.²³
- Step 3: Create a tetrahedron mesh for the entire domain and take the barycenter of the elements as the material points and the vertices as nodes in the HOTM method. Figure 2 shows an example of the triangulation of a powder bed as well as the HOTM discretization. Powders with bad quality, such as hollow spheres and particles with a rough surface or a crack as observed in experiments, can also be inserted into the powder bed.

3 | NUMERICAL METHOD

3.1 | General computational framework

For the sake of completeness, the construction of the HOTM method for materials in extreme thermomechanical coupling conditions proposed by Wang et al⁴³ is briefly introduced in this section. The HOTM method is an incremental Lagrangian method. The framework combines the OTM method and the extension of the variational formulation proposed by Stainier⁴⁶ for thermomechanical coupling problems by accounting for phase transition and inertia effect. The evolution of deformation, local state variables, and temperature distribution in the computational domain are predicted by solving the fully discretized governing equations using an explicit-implicit method.

FIGURE 1 The process of the DEM simulation. (A) Packaging density 5%. (B) Packaging density 22%. (C) Packaging density 55%

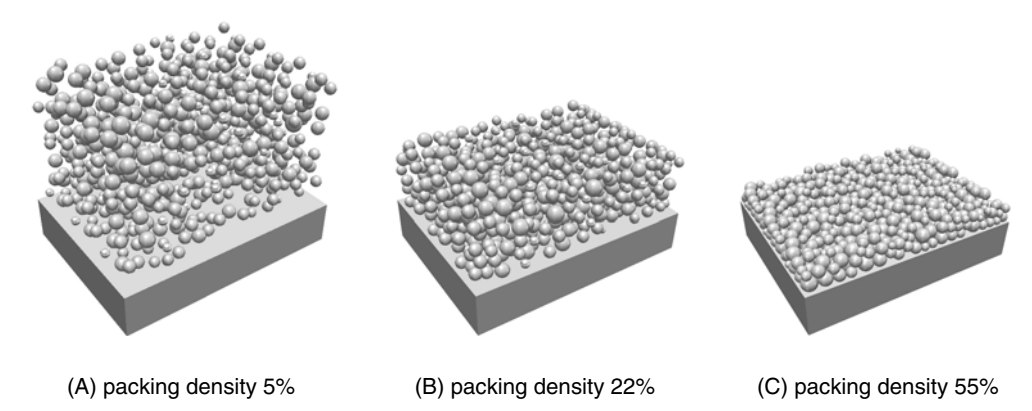
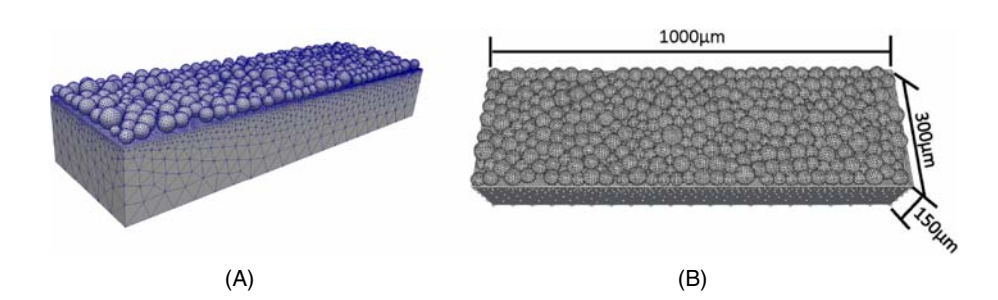


FIGURE 2 (A) The triangulation of a powder bed geometry constructed from DEM results and (B) its meshfree discretization [Color figure can be viewed at wileyonlinelibrary.com]



We consider a thermomechanical problem defined on a continuous body in the reference configuration $\Omega_0 \subset \mathbb{R}^3$ and the time interval [0,t]. The deformation mapping $\varphi: \Omega_0 \times [0,t] \to \mathbb{R}^3$ describes the motion of the body. A material point $X \in \Omega_0$ in the reference configuration is mapped to a point $\mathbf{x} = \varphi(X,t)$ in the spatial configuration $\Omega_t = \varphi(\Omega_0,t)$. Suppose for the deformation variable, the boundary $\partial\Omega_0$ is the disjoint union of a displacement boundary Γ_u and a traction boundary Γ_t . For the temperature, the boundary $\partial\Omega_0$ is decomposed into a temperature boundary Γ_t and a heat flux boundary Γ_t . Dynamic thermal and mechanical equilibrium of a thermomechanical system with general dissipative mechanisms is enforced weakly by recourse to the variational framework⁴⁵

$$\Phi[\dot{\boldsymbol{\varphi}},T,\dot{\boldsymbol{Z}}] = \int_{\Omega_0} (\dot{K} + \dot{\mathcal{W}}) dV - \int_{\Omega_0} \rho_0 \boldsymbol{B} \cdot \dot{\boldsymbol{\varphi}} dV - \int_{\Gamma_t} \overline{\mathbf{T}} \cdot \dot{\boldsymbol{\varphi}} dA + \int_{\Omega_0} \rho_0 Q(t) \log \frac{T}{T_0} dV - \int_{\Gamma_q} \overline{h}(t) \log \frac{T}{T_0} dA, \tag{1}$$

where K is the kinetic energy density, W is the effective energy density, W is the body force per unit mass, \overline{T} is the external traction, Q is the heat source, and \overline{h} is the outward heat flux.

The state variables within our numerical framework are the deformation φ , the temperature T, and the internal variable Z. The deformation gradient F is defined as $F(X,t) = \nabla_0 \varphi(X,t)$, where ∇_0 donates the partial derivatives of the motion with respect to the reference configuration. Following the framework of Stainier, ⁴⁶ we assume the existence of a Helmholtz free energy density A(F,T,Z) and a dissipation pseudo-potential $\Delta(\dot{F},\dot{Z},G;F,Z,T)$. The Helmholtz free energy density is further decomposed additively as

$$A = W^{e,vol}(J,T) + W^{e,dev}(\mathbf{F},T) + W^p(\mathbf{Z},T) + W^h(T), \tag{2}$$

where $J=\det {\bf F}$ is the Jacobian, a measurement of the volumetric deformation. $W^{e,\,vol}$ and $W^{e,\,dev}$ denote the strain energy density related to the volumetric and deviatoric thermoelastic responses of the material upon unloading, respectively, whereas W^p represents the stored energy density due to an internal process, such as plasticity, and W^h describes the heat storage in the material from the heat capacity. The exact forms of $W^{e,\,vol}$, $W^{e,\,dev}$, W^p , and W^h depend on specific material models. Similarly, the dissipation pseudo-potential $\Delta(\dot{F},\dot{Z},G;F,Z,T)$ can be decomposed into three parts as

$$\Delta(\dot{\mathbf{F}}, \dot{\mathbf{Z}}, \mathbf{G}; \mathbf{F}, \mathbf{Z}, T) = \phi^* + \psi^* - \chi, \tag{3}$$

where $G = -\frac{1}{T}\nabla_0 T$ is a parameter, $\phi^*(\dot{F}; F, T, Z)$ denotes the viscous dissipation, $\psi^*(\dot{Z}; F, T, Z)$ is a kinetic dissipation pseudo-potential related to internal processes, and $\chi(G; F, T, Z)$ represents the dissipation of heat conduction. Finally, the effective energy density W in Equation (1) takes the form

$$\dot{\mathcal{W}} = \dot{A} + \eta \dot{T} + \Delta (\frac{T}{\Theta} \dot{F}, \frac{T}{\Theta} \dot{Z}, G), \tag{4}$$

where η is the specific entropy and Θ is a state function derived from the internal energy through $\Theta(F, T, \mathbf{Z}) = \partial U/\partial \eta$. Therefore Θ can be treated as the internal temperature field, whereas T is the external temperature field. Θ is identical to T under thermal equilibrium condition.

The work conjugates to F, and T are the first Piola-Kirchhoff stress tensor P and the heat flux q, respectively. We assume there exists a force Y that is conjugate to the internal variable Z. Additionally, the conjugate forces can be decomposed into equilibrium and dissipative part additively, such that $P = P^e + P^v$ and $Y = Y^e + Y^d$. By Coleman's relations, the entropy, heat flux and forces conjugate to state variables can be derived as

$$\eta = -\frac{\partial A}{\partial T}(\mathbf{F}, T, \mathbf{Z}),\tag{5}$$

$$q = \frac{\partial \Delta}{\partial G}.$$
 (6)

and

$$\boldsymbol{P}^{e} = \frac{\partial A}{\partial \boldsymbol{F}}(\boldsymbol{F}, T, \boldsymbol{Z}),\tag{7}$$

$$\mathbf{Y}^{e} = \frac{\partial A}{\partial \mathbf{Z}}(\mathbf{F}, T, \mathbf{Z}),\tag{8}$$

$$\boldsymbol{P}^{\nu} = \frac{\partial \Delta}{\partial \dot{\boldsymbol{F}}} (\dot{\boldsymbol{F}}; \boldsymbol{F}, T, \boldsymbol{Z}), \tag{9}$$

$$\mathbf{Y}^{d} = \frac{\partial \Delta^{*}}{\partial \dot{\mathbf{Z}}} (\dot{\mathbf{Z}}; \mathbf{F}, T, \mathbf{Z}), \tag{10}$$

respectively. The solution $\{\dot{\boldsymbol{\varphi}}, T, \dot{\boldsymbol{Z}}\}$ of a thermomechanical system can be obtained from the extrema conditions of the variational formulation, such that

$$\inf_{\dot{\boldsymbol{\phi}}} \sup_{T} \inf_{\dot{\boldsymbol{Z}}} \Phi[\dot{\boldsymbol{\varphi}}, T, \dot{\boldsymbol{Z}}]. \tag{11}$$

From the Euler-Lagrangian equations of the variational structure Φ , we obtain the following conservation laws and balance equations in the Lagrangian description for a finite deformation problem,

$$\rho_0 \ddot{\boldsymbol{\varphi}} = \nabla_0 \boldsymbol{P} + \rho_0 \boldsymbol{B},\tag{12}$$

$$\mathbf{P}\mathbf{F}^{T} = \mathbf{F}\mathbf{P}^{T},\tag{13}$$

$$T\dot{\eta} = \mathbf{P}^{\nu} : \dot{\mathbf{F}} + \mathbf{Y}^{d} \cdot \dot{\mathbf{Z}} - \nabla \cdot \mathbf{q} + \rho_{0}Q, \tag{14}$$

and the boundary conditions are

$$\varphi(X, t) = \overline{\varphi}(X, t) \quad \text{on } \Gamma_u \times [t_0, t]$$
 (15)

$$\mathbf{P} \cdot \hat{\mathbf{N}} = \overline{\mathbf{T}} \quad \text{on } \Gamma_t \times [t_0, t]$$
 (16)

$$T(\mathbf{X}, t) = \overline{T}(\mathbf{X}, t) \quad \text{on } \Gamma_T \times [t_0, t]$$
 (17)

$$\overline{h} = \boldsymbol{q} \cdot \hat{\boldsymbol{N}} \quad \text{on } \Gamma_q \times [t_0, t],$$
 (18)

where ρ_0 denotes the density in the reference configuration, \hat{N} is the outward normal direction, $\overline{\varphi}$ and \overline{T} are the applied displacement and temperature on the boundary, respectively. The mass conservation is enforced by the density $\rho = \rho_0/J$. Since we do not allow mass transport in the Lagrangian configuration, the mass conservation or continuity equation is satisfied trivially.

To compute the time evolution of the state variables, the variational formulation Φ can be reduced to a series of incremental problems characterized by an optimization principle. For a given time interval $[t_n, t_{n+1}]$, the state variables $\{\varphi_{n+1}, T_{n+1}, Z_{n+1}\}$ at time t_{n+1} can be approximated through the state variables $\{\varphi_n, T_n, Z_n\}$ at time t_n by the minimization of the incremental energy, that is, minimizing all admissible paths from $\{\varphi_n, T_n, Z_n\}$ to $\{\varphi_{n+1}, T_{n+1}, Z_{n+1}\}$ as

$$\Phi_n[\boldsymbol{\varphi}_{n+1}, T_{n+1}, \boldsymbol{Z}_{n+1}] = \inf_{\text{paths}} \int_{t_{-}}^{t_{n+1}} \Phi[\dot{\boldsymbol{\varphi}}, T, \dot{\boldsymbol{Z}}] dt.$$
 (19)

The internal variable Z_{n+1} can be obtained by applying the extrema condition to the incremental variational potential. Therefore, $\Phi_n[\varphi_{n+1}, T_{n+1}, Z_{n+1}]$ is simplified to $\Phi_n[\varphi_{n+1}, T_{n+1}]$. By using the optimal transportation theory for the approximation of the kinetic energy from t_n to t_{n+1} and the backward Euler method for the rest of the terms in $\Phi_n[\varphi_{n+1}, T_{n+1}]$, ⁴⁴ the semi-discretized incremental variational formulation is of the form

$$\mathcal{I}_{n}[\boldsymbol{\varphi}_{n+1}, T_{n+1}] = \frac{1}{2} \frac{d_{W}^{2}(\rho_{n}, \rho_{n+1})}{\Delta t} + \int_{\Omega_{n}} (\mathcal{W}_{n+1}^{*} - \mathcal{W}_{n}) dV
- \int_{\Omega_{n}} \rho_{n} \boldsymbol{B}_{n+1} \cdot \Delta \boldsymbol{\varphi} dV - \int_{\Gamma_{t}} \overline{T}_{n+1} \cdot \Delta \boldsymbol{\varphi} dA
+ \int_{\Omega_{n}} \rho_{n} Q_{n+1} \log \frac{T_{n+1}}{T_{n}} \Delta t dV
- \int_{\Gamma_{q}} \overline{h}_{n+1} \log \frac{T_{n+1}}{T_{n}} \Delta t dA,$$
(20)

where d_W^2 is the Wasserstein distance.⁴⁴

The Ritz-Galerkin approach is employed to construct the spatial discretization of the incremental potential. The approximated admissible subspace \mathcal{V}^h generated on a given spatial discretization \mathcal{T}^h of Ω_0 can be derived as

$$\mathcal{V}^{h} = \{ \boldsymbol{\varphi}^{h} : \Omega_{0} \times [t_{0}, t] \to \Re^{3} | \boldsymbol{\varphi}^{h}(\boldsymbol{X}, t) = \sum_{a=1}^{N} \boldsymbol{x}_{a}(t) N_{a}(\boldsymbol{X}),$$

$$\mathcal{T}^{h} : \Omega_{0} \times [t_{0}, t] \to \Re^{+} | T^{h}(\boldsymbol{X}, t) = \sum_{a=1}^{N} T_{a}(t) N_{a}(\boldsymbol{X}) \},$$
(21)

where $\mathbf{x}_a = \boldsymbol{\varphi}(\mathbf{X}_a, t)$ and $T_a = T(\mathbf{X}_a, t)$ are the current position and temperature of a node a in \mathcal{T}^h , respectively. N is the dimension of the discretization of \mathcal{T}^h . N_a denotes the shape function associated with node \mathbf{x}_a at time t. In the HOTM framework, the LME meshfree approximation scheme⁶¹ is applied to acquire the capability of simulating large deformations for materials under extreme thermomechanical conditions. The LME shape functions have a number of advantages, such as the weak Kronecker-Delta property, finite element compatibility, and robust and efficient solution scheme, and so on.⁶¹ Thus, the incremental deformation mapping $\boldsymbol{\varphi}_{n \to n+1}$ from time t_n to t_{n+1} and the current temperature T_{n+1} at an arbitrary location \boldsymbol{x}_n can be approximated as

$$\mathbf{x}_{n+1} = \boldsymbol{\varphi}_{n \to n+1}(\mathbf{x}_n) = \sum_{a \in \mathcal{A}} \mathbf{x}_{a,n+1} N_a(\mathbf{x}_n),$$
 (22)

$$T_{n+1}(\mathbf{x}_n) = \sum_{a \in A} T_{a,n+1} N_a(\mathbf{x}_n), \tag{23}$$

where $x_{a,n+1}$ and $T_{a,n+1}$ are the position and temperature of the node x_a at time t_{n+1} , respectively. A is an index set of nodes whose support of the shape function covers the point x_n at time t_n .

As shown in Figure 3, the computational domain in the HOTM method is discretized by adopting the usual Lebesgue measure L of the volume as a sum of material points following

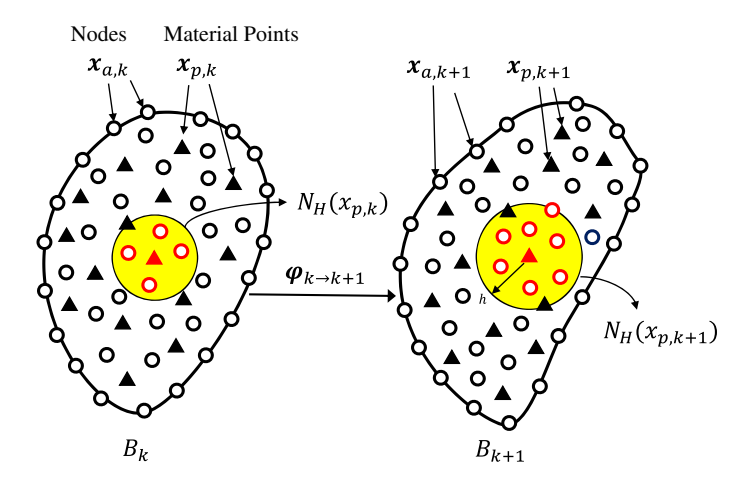


FIGURE 3 Schematic of the HOTM approximation scheme [Color figure can be viewed at wileyonlinelibrary.com]

$$L_n^h = \sum_{n=1}^M v_{p,n} \delta(\mathbf{x} - \mathbf{x}_{p,n}), \tag{24}$$

where $v_{p,n}$ is the volume of a material point $\mathbf{x}_{p,n}$ and M is the number of material points in the domain. All the field information is carried by the nodes and material points. Particularly, the node $\mathbf{x}_{a,n}$ carries the kinematic information, such as displacement, velocity, and acceleration, while the local states of materials, such as strain, stress, material properties, and internal variables are evaluated at the material points $\mathbf{x}_{p,n}$. The material point sampling supplies an efficient way for numerical integration without a background mesh. The location, temperature, deformation gradient, and temperature gradient at a material point at time t_{n+1} are interpolated from the nodes within its neighborhood $N_H(\mathbf{x}_{p,n})$ established at time t_n . Figure 3 also indicates the connection between material points and nodes is dynamically reconstructed on-the-fly by a search algorithm based on the local deformation at each time step. Unlike the conventional Lagrangian FEM where the shape functions are only evaluated once in the reference configuration, the dynamic connectivity between material points and nodes in the HOTM method requires recalculation of the shape functions in the current configuration at each time step.

Finally, applying the discrete measures to the incremental variational formulation $\mathcal{I}_n[\varphi_{n+1}, T_{n+1}]$, and imposing stationarity conditions yield the fully discrete mechanical and thermal balance equations

$$\mathbf{f}_{a,n+1}^{\text{int}} - \mathbf{f}_{a,n+1}^{\text{ext}} = m_{a,n+1} \ddot{\boldsymbol{\varphi}}_{a,n+1}, \tag{25}$$

$$Q_{a,n+1}^{\text{int}} - Q_{a,n+1}^{\text{ext}} = 0, (26)$$

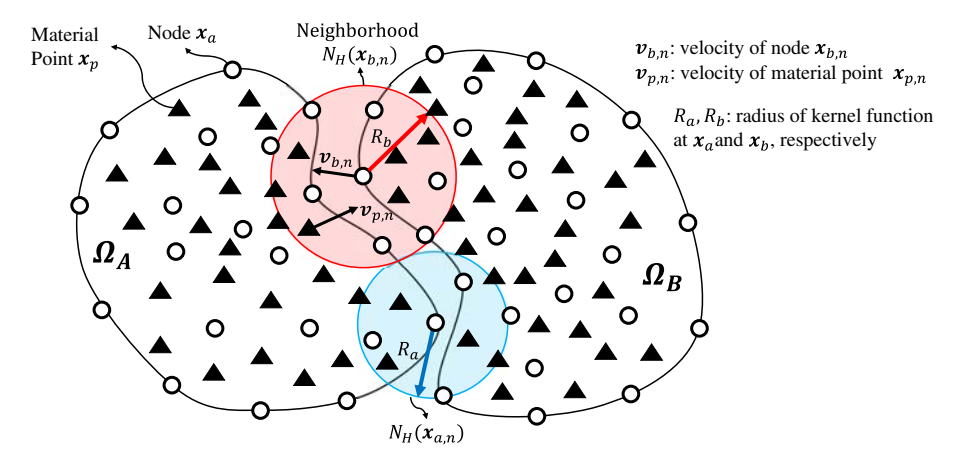
where $m_{a,n+1}$ is the lumped mass of a node x_a interpolated from the mass of material points in its support $N_H(x_{a,n})$, and $\ddot{\varphi}_{a,n+1}$ is the nodal acceleration approximated using a central difference scheme at time t_{n+1} (see the Appendix for detail).

We employ a split algorithm to solve the system of balance equations (A1) and (A2). Based on the expression of the discretized form of the variational potential, an explicit solution scheme can be applied to solve the mechanical balance equation (A1), where the well-known Courant-Friedrichs-Lewy (CFL) conditions require the time step size to be small enough to maintain a stable solution. Nevertheless, the time scale for heat transfer is usually much longer than the one restricted by the CFL conditions. Therefore, an operator splitting algorithm is taken to decouple the solution procedure, and the thermal balance equation (A2) is solved by an implicit method. To be specific, the mechanical balance equation is solved at a constant temperature obtained from the previous iteration of the thermal equation, while the thermal balance equation is solved at the fixed deformed configuration obtained from the last iteration of the mechanical equation. The mechanical and thermal iterations proceed until the total simulation time is reached.

3.2 Meshfree contact algorithm

The contact forces and heat conduction between discrete particles and particle/substrate are modeled by the OTM contact algorithm.⁶² Within a meshfree setting, the linear momentum of node x_a at time t_n can be approximated from the

FIGURE 4 Schematic of the OTM contact algorithm and the support of nodes [Color figure can be viewed at wileyonlinelibrary.com]



neighboring material points x_p by

$$\mathbf{l}_{a,n} = \sum_{\mathbf{x}_{p,n} \in N_H(\mathbf{x}_{a,n})} \mathbf{l}_{p,n} N_a(\mathbf{x}_{p,n}) = \sum_{\mathbf{x}_{p,n} \in N_H(\mathbf{x}_{a,n})} m_p \frac{\mathbf{x}_{p,n} - \mathbf{x}_{p,n-1}}{t_n - t_{n-1}} N_a(\mathbf{x}_{p,n}),$$
(27)

where the support or neighborhood of the node is $N_H(\mathbf{x}_a) = \{\mathbf{x} \in \Omega, |\mathbf{x} - \mathbf{x}_a| \leq R\}$ and R is the radius of the kernel function. At the end of time step t_n , the support size R is updated according to the local deformation, for instance, $R_{n+1} = (J_{n \to n+1})^{1/d} R_n$ where $J_{n \to n+1}$ is the Jacobian of the incremental deformation. The neighborhood of the nodes is rebuilt using a search algorithm, and the shape functions are re-calculated in the current configuration. In specific, the contact searching is accomplished by using a cell structure that is fixed in space, and the cell sizes are considered to be a multiple of the kernel radius. The global searching takes a computational cost in the order of O(N), where N is the total number of nodes from multiple bodies, to find all candidate material points in support of a node. Suppose two bodies Ω_A and Ω_B are undergoing a motion which conserves linear momentum, material points belonging to Ω_A may move to the vicinity of a node on Ω_B at time step t_{n+1} .

As shown in Figure 4, the material point $x_p \in \Omega_A$ is concerned as a neighboring material point of the node $x_a \in \Omega_B$ when,

$$(\mathbf{v}_{a,n+1} - \mathbf{v}_{p,n+1}) \cdot (\mathbf{x}_{p,n+1} - \mathbf{x}_{a,n+1}) > 0. \tag{28}$$

Thus, the linear momentum of node x_a at time t_{n+1} can be rewritten as

$$\boldsymbol{l}_{a,n+1} = \sum_{\substack{x_{p,n+1} \in \\ N_H(x_{a,n+1}) \cap \Omega_R}} \boldsymbol{l}_{p,n+1} N_a(\boldsymbol{x}_{p,n+1}) + \sum_{\substack{x_{q,n+1} \in \\ N_H(x_{a,n+1}) \cap \Omega_A}} \boldsymbol{l}_{q,n+1} N_a(\boldsymbol{x}_{q,n+1}).$$
(29)

The rate of linear momentum change of node x_a from time t_n to t_{n+1} may be obtained by subtracting Equation (27) from Equation (29), with the result,

$$\frac{\mathbf{l}_{a,n+1} - \mathbf{l}_{a,n}}{t_{n+1} - t_n} = (\mathbf{f}_{a,n+1}^{\text{ext}} - \mathbf{f}_{a,n+1}^{\text{int}}) + \mathbf{f}_{a,n+1}^{e},$$
(30)

where

$$\mathbf{f}_{a,n+1}^{c} = \frac{\sum_{\mathbf{x}_{q,n+1} \in N_{H}(\mathbf{x}_{a,n+1}) \cap \Omega_{A}} \mathbf{l}_{q,n+1} N_{a}(\mathbf{x}_{q,n+1})}{t_{n+1} - t_{n}},$$
(31)

is the contact force concentrated at the contact nodes induced by linear momentum gained from neighboring material points on a different body. The OTM contact algorithm is convenient to implement within the Lagrangian framework and introduces no extra computational cost to the simulation since the neighbor search is already conducted to determine the mesh-free shape functions. Although the nonpenetration constraint in conventional contact approaches is not

enforced in the OTM contact algorithm, it allows for mixing of materials at the interface and may serve the purpose to simulate the merging of melted particles. Note that the OTM contact algorithm is a seizing contact algorithm and does not allow for sliding. That means, as a node from Ω_B becomes the neighbor of a material point in Ω_A , it sticks to Ω_A eventually and the friction between the two contact bodies tends to be infinite. Other meshfree contact algorithms may also be considered in the HOTM framework, such as node to node contact algorithm proposed for the SPH method.⁶³

3.3 | Artificial viscosity

To improve the stability of the numerical solutions of unconstrained solid and fluid flow, the Lagrangian artificial viscosity scheme proposed by Lew and Ortiz⁶⁴ is introduced to the HOTM method. Besides the physical viscosity coefficient ν of the material, an artificial viscosity term $\Delta \nu$ is added to the system. Therefore, the total viscosity coefficient of a material point becomes

$$v_{total} = v + \Delta v, \tag{32}$$

where the artificial viscosity coefficient Δv is defined as

$$\Delta v = \begin{cases} \max\left(0, \frac{3}{4}h\rho(c_1c_s - c_2\Delta u) - v\right), & \Delta u < 0\\ 0, & \Delta u \ge 0, \end{cases}$$
(33)

and h is a measurement of the material point size, c_s is the characteristic sound speed of the material, Δu measures the velocity jump at the material point, and c_1 and c_2 are coefficients determined by numerical experiments. In our calculations, we choose $c_1 = 0.1$, $c_2 = 1.0$. Although the added artificial viscosity stabilized the meshfree computation by using large values for c_1 and c_2 , it leads to in-physical results in the Lagrangian simulation of fluid flow in presence of excessive localized deformations, such as small-scale vortices and turbulence. Additionally, evaluation of the jump in velocity is not straightforward in a three-dimensional problem involving incompressibility and rigid body rotation. An incrementally objective and volume preserving approximation of the velocity jump at a material point at time t_{n+1} takes the form

$$\Delta u_{n+1} = h_{n+1} \text{tr} \boldsymbol{d}_{n+1} = \frac{h_{n+1}}{2\Delta t} \text{tr}(\log(\boldsymbol{F}_{n \to n+1} \boldsymbol{F}_{n \to n+1}^T)), \tag{34}$$

where $F_{n \to n+1}$ is the deformation gradient of the incremental motion $\varphi_{n \to n+1}$ and the rate of deformation tensor d is measured as one-half the *Lie derivative* of the spatial metric.⁶⁵

3.4 | Material model for metallic powder particles

In response to the high energy input of the laser beam, the powder particles experience a complex thermal history with melting, vaporization, and solidification. To predict the stress developed in the powder material during the multiphase transition, a phase-aware thermomechanical constitutive model must be developed. Within the HOTM framework, the temperature T is defined as a local state variable to determine the phase of a material point. In specific, a material point is in a solid phase if its local temperature is lower than the melting temperature. As the temperature exceeds the melting or boiling temperature, the state of the material point transforms into the liquid or gas phases automatically. In addition, parameters in the material models must be considered as functions of temperature.

While extremely large deformation is involved at the material points in PBF AM processes and the deformation gradient becomes very large in the fluid flow, the finite deformation problem can be described as a sequence of small strain problems with the aid of our incremental framework and the logarithmic transformation

$$\varepsilon_{n+1} = \frac{1}{2} \log(\mathbf{F}_{n+1}^T \mathbf{F}_{n+1}),$$
 (35)

where ε_{n+1} is the small strain tensor at time t_{n+1} .⁶⁶ Since metal materials soften and may yield at temperature close to melting temperature, the magnitude of recoil pressure due to vaporization may induce plastic deformation in the solid particles before phase transition, which affects the motion and dynamic contacts in the powder bed. As observed in experiments, contact between discrete particles determines the heat conductivity in the powder bed, and controls the deformed configuration and dynamics of the melt pool. Thus, we consider the thermal viscoplasticity model for particles in the solid phase and thermal viscoelasticity as they melt. To this end, we follow the multiplicative elastic-plastic kinematics suggested by Lee⁶⁷ to decompose the deformation gradient as

$$F = F^{e}F^{p}, \tag{36}$$

where F^e and F^p are the elastic and plastic deformation, respectively. The logarithmic elastic strain tensor takes the form

$$\boldsymbol{\varepsilon}^{\mathrm{e}} = \frac{1}{2} \log(\boldsymbol{F}^{\mathrm{e}T} \boldsymbol{F}^{\mathrm{e}}). \tag{37}$$

We then introduce a scalar internal variable, $\overline{\epsilon}^p$, to measure the cumulated plastic strain in a macroscopic plasticity model of the von Mises type. The plastic flow rule for von Mises plasticity can be stated as

$$\boldsymbol{L}^{p} = \dot{\boldsymbol{F}}^{p} \boldsymbol{F}^{p-1} = \dot{\overline{\epsilon}}^{p} \boldsymbol{M}, \tag{38}$$

where the direction tensor M is a symmetric tensor such that the normalization conditions and isochoricity of plastic flow are satisfied, that is,

$$\mathbf{M} \cdot \mathbf{M} = \frac{3}{2}$$
 and $tr[\mathbf{M}] = 0.$ (39)

The volumetric and deviatoric elastic deformation, the stored plastic work and heat capacity in Equation (2) for metallic particles under high power beam scanning are described by the following energy densities,⁶⁸

$$W^{e, \text{vol}}(J, T) = \frac{K(T)}{4} [J^{2} - 2(1 + 3a(T)\Delta T) \log J - 1],$$

$$W^{e, \text{dev}}(F, T) = \mu(T) \|\epsilon^{e, \text{dev}}\|^{2},$$

$$W^{p}(\overline{\epsilon}^{p}, T) = \frac{n\sigma_{0}\overline{\epsilon}_{0}^{p}}{n+1} \left(1 + \frac{\overline{\epsilon}^{p}}{\overline{\epsilon}_{0}^{p}}\right)^{\frac{n+1}{n}} \left(1 - \frac{T - T_{0}}{T_{m} - T_{0}}\right)^{l},$$

$$W^{h}(T) = C(T) \left(T - T_{0} - T \log \frac{T}{T_{0}}\right),$$
(40)

where the deviatoric part of the small strain tensor is defined as $\varepsilon^{\rm e,dev} = \varepsilon^{\rm e} - \frac{1}{3} {\rm tr} \varepsilon^{\rm e} {\it I}$, σ_0 denotes the initial yield stress, $\overline{\varepsilon}_0^p$ is the reference effective plastic strain, n>1 is the hardening exponent, and K(T), a(T), $\mu(T)$, and C(T) are the temperature-dependent bulk modulus, linear thermal expansion coefficient, shear modulus, and heat capacity per unit undeformed volume of the material, respectively. The plastic work vanishes and the plastic strains are relaxed once the local temperature reaches the melting temperature. Consequently, as the material melts or vaporizes, the local Helmholtz free energy density automatically changes to be of the simple form

$$A = W^{\text{e,vol}}(J, T) + W^{h}(T), \tag{41}$$

which represents the compressible response of the liquid or gas phase as an appropriate equation of state is employed.

To compute the heat generated/sink during the phase transition process, the apparent heat capacity method is employed.⁶⁹ Suppose the phase transition temperature is T_p , the specific heat capacity coefficient C(T) can be enlarged to incorporate the latent heat in a small temperature interval ΔT , that is, $T \in [T_p - \Delta T, T_p + \Delta T]$, assuming the form

$$C(T) = C_{\text{phase1}}[1 - \alpha(T)] + C_{\text{phase2}}\alpha(T) + \rho_0 L \frac{d\alpha}{dT},$$
(42)

where C_{phase1} and C_{phase2} denote the heat capacity coefficient of phase 1 and 2, respectively. L is the latent heat of the material as it transforms from phase 1 to phase 2. $\alpha(T)$ is introduced to represent the smooth transition between phase 1 and phase 2 in the phase transition temperature interval, which can be stated as

$$\alpha(T) = \frac{1}{2} \left[1 + \operatorname{erf}\left(\frac{T - T_p}{\sqrt{2}\sigma}\right) \right],\tag{43}$$

where σ is the standard deviation of the transition zone. Thus its derivative is obtained as

$$\frac{\mathrm{d}\alpha}{\mathrm{d}T} = \frac{1}{\sqrt{2\pi\sigma}} \exp\left[-\frac{(T-T_p)^2}{2\sigma^2}\right]. \tag{44}$$

Furthermore, the dissipation pseudo-potential consists of two parts due to the viscosity of the material and the heat conduction. We consider Newtonian fluid such that the viscous dissipation pseudo-potential $\phi^*(\dot{F}; F, T, Z)$ takes the particular form

$$\phi^* = \nu(T) \mathbf{d}^{\text{dev}} : \mathbf{d}^{\text{dev}}, \tag{45}$$

where v(T) is the temperature-dependent shear viscosity coefficient, $\mathbf{d} = sym(\dot{\mathbf{F}}\mathbf{F}^{-T})$ is the rate of deformation tensor, $\mathbf{d}^{\text{dev}} = \mathbf{d} - \frac{1}{2}tr(\mathbf{d})\mathbf{I}$ is its deviatoric component.

The Fourier law leads to the simple form for the dissipation potential due to heat conduction as

$$\chi(G; F, Z, T) = \frac{1}{2}\kappa(T)TG^{2}, \tag{46}$$

and the Fourier heat flux is obtained as

$$\mathbf{q} = \frac{\partial \chi}{\partial \mathbf{G}} = \kappa(T)T\mathbf{G} = -\kappa(T)\nabla_0 T,\tag{47}$$

where

$$\kappa(T) = \kappa_{phase1}[1 - \alpha(T)] - \kappa_{phase2}\alpha(T), \tag{48}$$

is the heat conductivity coefficient as a function of temperature with a smooth transition in the transition temperature interval described by the function $\alpha(T)$.

Finally, according to the Coleman's relation, the cauchy stress in the material yields

$$\sigma = J^{-1} \left(\frac{\partial A}{\partial F} + \frac{\partial \phi^*}{\partial \dot{F}} \right) F^T$$

$$= p(J, T) \mathbf{I} + 2\mu(T) \varepsilon^{\text{dev}} + 2\nu(T) \mathbf{d}^{\text{dev}}, \tag{49}$$

where the pressure is given by

$$p(J,T) = \frac{K(T)}{2} \left[J - (1 + 3a(T)\Delta T) \frac{1}{J} \right]. \tag{50}$$

As the material point in the solid state, accounting for the flow rule (38), the plastic deformation of the powder particles is driven by the conjugate force

$$Y = \overline{\sigma} - \sigma_c, \tag{51}$$

where we have the effective von-Mises stress defined as

$$\overline{\sigma} = \sqrt{\frac{3}{2}\sigma^{\text{dev}} : \sigma^{\text{dev}}},\tag{52}$$

and the flow stress with strain hardening and thermal softening is derived from the plastic work in Equation (40), namely,

$$\sigma_c = \frac{\partial W^p}{\partial \overline{\epsilon}^p} = \sigma_0 \left(1 + \frac{\overline{\epsilon}^p}{\overline{\epsilon}_0^p} \right)^{\frac{1}{n}} \left(1 - \frac{T - T_0}{T_m - T_0} \right)^l.$$
 (53)

Note that Equation (49) is derived for a general continuum media, either solid or fluid flow. Thus, the general constitutive relation is employed to calculate the stress of the material regardless of its phase. Nevertheless, the dynamic response of the material is intimately related to its local state. The phase change of the material, such as the melting and solidification process, maybe modeled continuously by varying its macroscopic responses. However, instead of changing the constitutive relation itself, in this model, critical is the determination of the C^0 continuous temperature functions of the material constants, such as K(T), $\mu(T)$, $\nu(T)$, and a(T), in different phases to guarantee the smooth transition of the stress during phase change. Consequently, as the temperature rises beyond the melting temperature, the material model automatically converts to the standard Newtonian viscous flow since the shear modulus $\mu(T)$ and plastic deformation vanishes, ⁴³ and

$$\sigma = p(J, T)\mathbf{I} + 2\nu(T)\mathbf{d}^{\text{dev}}.$$
(54)

In the fluid region, the liquid material is considered as a nearly incompressible fluid by taking a large bulk modulus K(T). The meshfree implementation of the algorithm enables us to overcome the difficulty of large deformation in the pure Lagrangian modeling of complex fluid flows.⁷⁰

3.5 | Boundary conditions of the powder bed

A variety of Neumann boundary conditions are applied to model the PBF based AM processes. First of all, a traction boundary condition is applied to the nodes at the free surface to simulate the vapor recoil pressure. The temperature-dependent recoil pressure proposed by Anisimov et al⁷¹ is employed to calculate the local traction, that is,

$$\overline{T}(T) = -0.54P_0 \exp\left[-\frac{\lambda}{K_B} \left(\frac{1}{T} - \frac{1}{T_b}\right)\right] \hat{N},\tag{55}$$

where P_0 is the ambient pressure, λ =4.3eV/atom is the evaporation energy per particle, K_B is Boltzmann constant, T is the surface temperature, T_b is the boiling temperature, and \hat{N} is the local normal direction of the free surface, respectively. The recoil pressure increases drastically when the melt pool temperature exceeds the boiling temperature, as indicated in Equation (55).

The effect of surface tension is taken into account as a traction boundary condition as well. The surface tension follows the conventional form 72

$$\overline{\mathbf{T}}(T) = -\sigma(T)\kappa\hat{\mathbf{N}},\tag{56}$$

where σ is the temperature-dependent surface tension coefficient, κ and \hat{N} are the surface curvature and normal direction, respectively. Within the Lagrangian framework, the free surface is tracked automatically without extra computational cost. However, it is cumbersome to build a surface representation explicitly in the meshfree simulations. We consider a nodal integration scheme to compute the external mechanical nodal forces due to the traction boundary conditions in Equation (A6) following

$$\mathbf{f}_{a,n+1}^{ext} = \overline{\mathbf{T}}_{a,n+1} A_{a,n}, \tag{57}$$

where $\overline{T}_{a,n+1}$ is the nodal traction, and the weight $A_{a,n}$ can be interpreted as the surface area of Γ_t tributary to node x_a . Nodes on the free surface in the reference configuration remain as surface nodes unless they are in contact with neighboring surface nodes. The surface area and normal direction of a free surface node x_a in the current configuration are determined by the Piola transformation incrementally,

$$A_{a,n+1}\hat{N}_{a,n+1} = J_{n \to n+1}F_{n \to n+1}^{-1}A_{a,n}\hat{N}_{a,n}, \tag{58}$$

where $J_{n \to n+1}$ and $F_{n \to n+1}$ are the incremental Jacobian and deformation gradient from t_n to t_{n+1} , respectively. The current curvature $\kappa_{a,n+1}$ of a surface node \mathbf{x}_a is determined following the approximation scheme proposed in Reference 73. In our calculations, a search algorithm is employed to find the surface neighborhood of \mathbf{x}_a , that is, $S_{n+1} = \{\mathbf{x}_{b,n+1} \in \Gamma, \text{s.t.} \mid \mathbf{x}_{b,n+1} - \mathbf{x}_{a,n+1} \mid \leq d\}$, where Γ is the free surface of the melted material. Thus, the normal curvature at \mathbf{x}_a with respect to individual neighboring nodes in S_{n+1} can be calculated as

$$\kappa_{i,n+1} = -\frac{(\mathbf{x}_{i,n+1} - \mathbf{x}_{a,n+1}) \cdot (\hat{\mathbf{N}}_{i,n+1} - \hat{\mathbf{N}}_{a,n+1})}{\|\mathbf{x}_{i,n+1} - \mathbf{x}_{a,n+1}\|^2}$$
where $\mathbf{x}_i \in S_{n+1}$. (59)

The principal curvatures, κ_1 and κ_2 at node \mathbf{x}_a , are then approximated by using the least square method from the set of individual curvatures $\{\kappa_{i,n+1}\}$. Finally, the current curvature is obtained as $\kappa_{a,n+1} = (\kappa_1 + \kappa_2)/2$.

Unlike the conventional approach, where the heat energy is simplified to a heat source model and applied over the whole layer to substitute the scanning path, the laser beam is applied to the surface of the powder bed as a heat flux boundary condition in our proposed framework. One of the most widely used heat flux models for laser beams in the field of AM takes the Gaussian distributed form:

$$\overline{h} = \frac{2AP}{\pi r^2} \exp\left[-2\frac{(x - x_c(t))^2 + (y - y_c(t))^2}{r^2}\right],\tag{60}$$

where A is the material absorptivity of the laser energy, P and r are the power and radius of the laser beam, respectively. The current location of the center of the laser beam can be manipulated by any time-dependent functions $x_c(t)$ and $y_c(t)$. It furnishes an effective means of controlling the movement and scanning strategies of the laser beam in the simulations. Thus, the influences of the scanning strategy, the laser power, shape, and other important processing parameters on the motion, deformation, and thermodynamics of the melt pool can be readily investigated within our framework.

The energy loss due to convective and radiation heat transfer from the powder bed to the atmosphere is another critical factor for cooling down the melt pool as observed in experiments. In the Lagrangian simulations, a convective heat flux boundary condition can be applied to the surface of the powder bed following the simple form

$$\overline{h} = \kappa_c (T - T_0), \tag{61}$$

where κ_c is the convective coefficient and T_0 is the temperature of the environment. The Stefan Boltzmann law is employed to model the radiation heat flux boundary condition, that is,

$$\overline{h} = \sigma \varepsilon (T^4 - T_0^4), \tag{62}$$

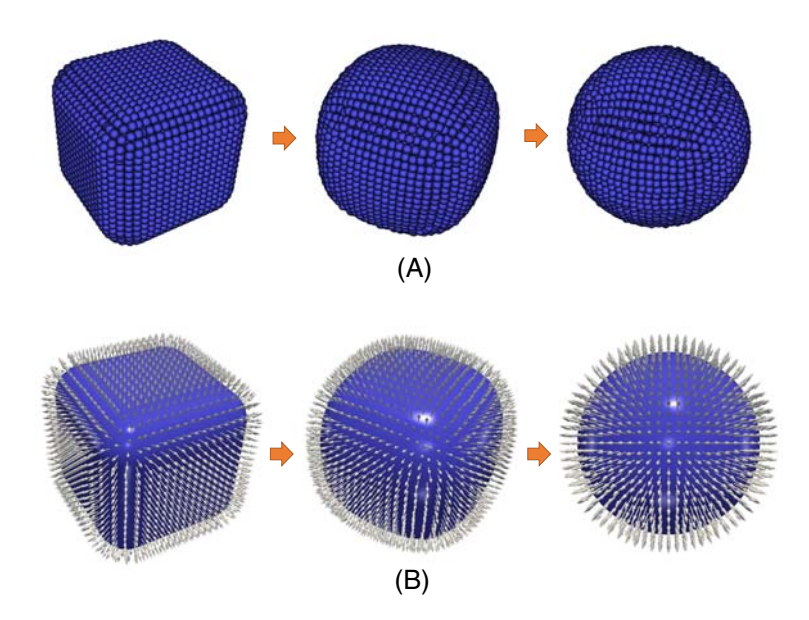
where $\sigma = 5.669~10^{-8}~W/m^2K^4$ is the Stephan constant and ε is the emissivity of the material. Similar to the external nodal mechanical forces, we consider the external thermal forces due to the heat flux boundary conditions are directly integrated at the surface nodes, which can be calculated as

$$Q_{a,n+1}^{ext} = \Delta t \frac{\overline{h}_{a,n+1}}{T_{a,n+1}} A_{a,n}. \tag{63}$$

TABLE 1 Material properties of Ti-6Al-4V

Density	Liquidus temperature	Latent heat of fusion	Surface tension coefficient
$4430 (kg/m^3)$	1883 (K)	360 (kJ/kg)	$1.53 (N/m)^{75}$

FIGURE 5 The deformation of a liquid cube to a sphere under the effect of surface tension [Color figure can be viewed at wileyonlinelibrary.com]



4 | VALIDATION

4.1 | Validation of surface tension

The surface tension plays an important role in the PBF AM processes. To show the accuracy of the meshfree calculation of surface tension, we conduct a standard benchmark test of a liquid droplet with an arbitrary initial shape transforming to a sphere under the effect of surface tension. The material of the droplet is melted Ti6Al4V with thermal and mechanical properties summarized in Figure 7 and Table 1.

The initial geometry of the droplet is a cube with fillets as shown in Figure 5. The length of the cube is 1 mm, and it is discretized by 7409 nodes and 38,048 material points within the HOTM framework. Figure 5A shows the deformed configuration of the droplet in a meshfree representation using nodes at different time steps predicted by the meshfree algorithm. Under the effect of surface tension applied as a traction boundary condition, the liquid cube transforms to an intermediate shape, and finally turns to a nearly perfect sphere as illustrated in Figure 5A. The evolution of the surface normal during the deformation of the droplet is demonstrated in Figure 5B. The initial volume of the geometry is 0.984 mm³. Thus, based on the nearly incompressible condition, the radius of a sphere with the same volume is R = 0.617 mm. The normalized L_2 error in the radius of the predicted final shape is computed by

$$||error||_{L_2} = \frac{||R^h - R||_{L_2}}{||R||_{L_2}},$$
 (64)

where

$$||R||_{L_2} = \sqrt{\int_{\Omega} R^2 dV}.$$
 (65)

The integrals are evaluated numerically by using the nodal integration. The normalized error is investigated for three different mesh sizes as shown in Figure 6. The error reduces from 1.17% to 0.68% as we refine the initial mesh of the domain by a factor of two. The accuracy of the meshfree computation of the surface tension is noteworthy in this verification example.

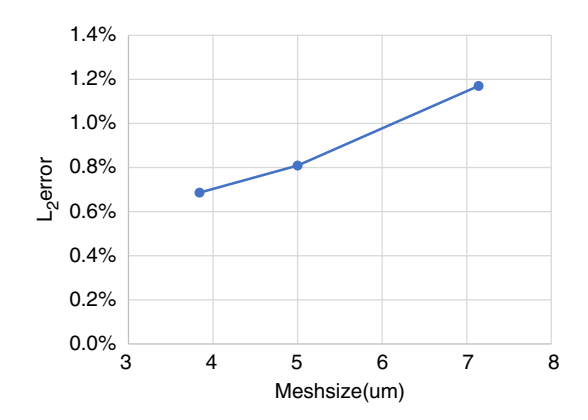


FIGURE 6 Convergence of the normalized error between the predicted radius of the final shape and the analytical solution in the meshfree computation of the surface tension [Color figure can be viewed at wileyonlinelibrary.com]

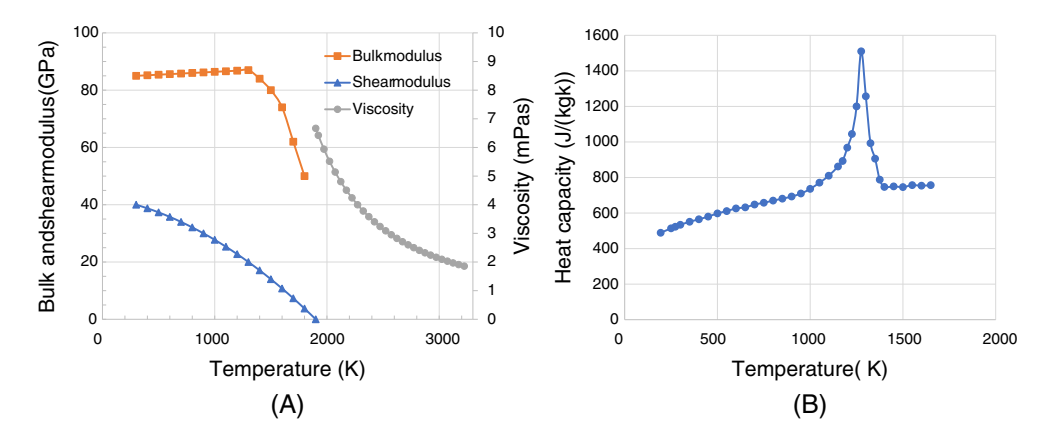


FIGURE 7 The (A) mechanical properties and (B) thermal properties of Ti6Al4V [Color figure can be viewed at wileyonlinelibrary.com]

4.2 | Validation of the PBF AM process

In this section, we validate the HOTM simulations of PBF AM processes at the powder-scale by comparing our predictions against the experimental tests of a single layer powder bed of Ti-6Al-4V in Dilip et al.⁴⁷ The diameters of the powder particles are ranged from 15 to 45 μ m with an average of 30 μ m. A single laser flux with a radius of 50 μ m is employed to conduct single-track depositions on the powder bed. The processing parameters investigated are laser power and scanning speed. In specific, the laser power of 50, 100, 150, and 195 W and laser moving speed of 0.5, 0.75, 1, and 1.2 m/s are investigated. The melt pool width and the porosity of the printed material are measured for each combination of the laser power and moving speed in the experiments.

In our simulations of the experimental configuration, a single-layered powder bed consisting of 312 particles on a substrate is created, as shown in Figure 2A. The diameters of the particles are initialized using a Gaussian distribution centered at 30 μ m. The powder beds' length and width are 1000 and 300 μ m, respectively. The height of the substrate is 150 μ m. The discretization of the powder bed geometry shown in Figure 2B shows the discretization of the powder bed and the substrate with 324,963 material points and 326,348 degrees of freedom. The temperature-dependent material properties of Ti6Al4V are illustrated in Figure 7A,B, including the bulk modulus, ⁷⁴ shear modulus, ⁷⁴ viscosity, ⁷⁵ and heat capacity. ⁷⁶ The experimental data of thermal conductivity can be found in literature.

A Gaussian distributed laser heat flux moving along the centerline of the powder bed is applied on the surface of the powder bed. Combinations of the laser moving speeds and laser powers in the experiments of Dilip et al⁴⁷ are studied by the HOTM numerical simulations. The radius of the laser beam is 50 μ m, which scans from the left to the right end of the domain. We consider a constant absorptivity coefficient A = 0.2 in Equation (60) as suggested in the review by King et al.¹ The emissivity of the material is 0.1, as measured from experiments. The other material properties are summarized in Table 1. The simulations are run parallelly on 30 Intel(R) Xeon(R) E5-2670 v3 cpus at the High Performance Computing Resource in the Core Facility for Advanced Research Computing at Case Western Reserve University. It takes about 35-84 hours to complete the 0.75-1.8 ms simulation time for different laser scanning speeds.

A typical simulation result of the PBF process is shown in Figure 8, in which the laser speed is 0.75 m/s and laser power is 100 W. The color indicates the temperature distribution in the powder bed and the melted material. To better

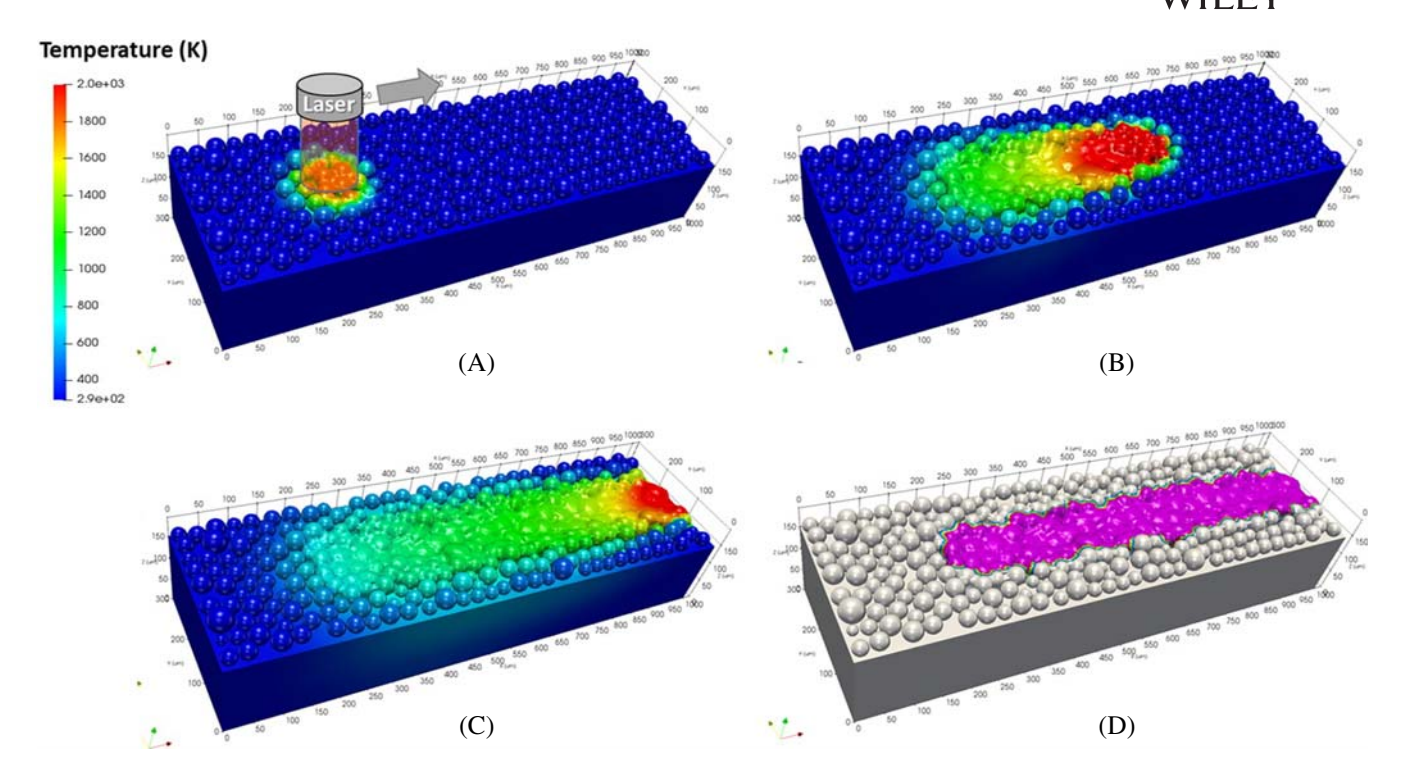


FIGURE 8 A typical simulation result of the PBF AM process for laser speed of 0.75 m/s and laser power 100 W. The color shows the temperature distribution in (A)-(C) and the purple color in (D) indicates the melted regime of the powder bed [Color figure can be viewed at wileyonlinelibrary.com]

demonstrate the melt pool, the simulation results are visualized in a solid representation using the initial connectivity of the nodes since there is a lack of surface representation in a meshfree manner. However, the connectivity table changes incrementally in the HOTM method. It may cause some visualization artifacts especially when melted particles are joining together and the initial connectivity is not valid anymore. It can be observed that a continuous melt pool is formed under the effect of recoil pressure and surface tension. The melt pool width measured from the simulation result in Figure 8 is $96.85 \mu m$, which is in an excellent agreement with the experimental measurement, $98 \mu m$.

The prediction of the average melt pool width and the final porosity of the melt track for various laser power and scanning speed are compared with experimental data in Dilip et al⁴⁷ to validate the HOTM simulations. It can be observed in Figure 9A that the simulation predictions of the melt pool width agree very well with experimental data with a maximum error of 12% at a laser power of 195 W and laser scanning speed at 0.5 m/s. As the laser moving speed increases, the melt pool width decreases both shown in the numerical simulations and experimental data. Figure 9B shows the relationship between the porosity of the solidified melt pool versus the volumetric energy density (VED) from simulations and experiments. The VED defined as $E_v = P/vht$ is a commonly used metric to optimize process parameters, where P is the laser power, v is the scanning speed, h is the hatching space (approximated by the laser diameter for single track), and tis the layer thickness, respectively.⁷⁷ It is evident that the porosity decreases as the VED increases. However, there exists a critical value of the VED beyond which the VED rise leads to higher porosity due to the keyhole formation. Again, the predicted correlation between the porosity and VED by the HOTM simulations is consistent with the data reported in experiments. The major discrepancy between simulations and experiments is found in the regime of high VED due to the activation of keyhole mode. The recoil pressure predicted in our simulations is not big enough to generate keyholes in the melt pool. On the other hand, the liquid metal is modeled as a nearly incompressible material. The slight compressibility of the domain also prohibits the massive distortion of the melt pool. There is also noticeable unrealistic fluid motion in the meltpool in the validation simulations as well as the numerical tests in the next section. The error is mainly caused by the artificial viscosity and the seizing contact algorithm. In order to stabilize the meshfree simulations, large values of the artificial viscosity coefficient were adopted resulting in a highly viscous flow. The seizing contact does not allow for sliding between mixing melted materials as well as solid-liquid interaction, which leads to dissipation numerical errors and further constrains the fluid motion.

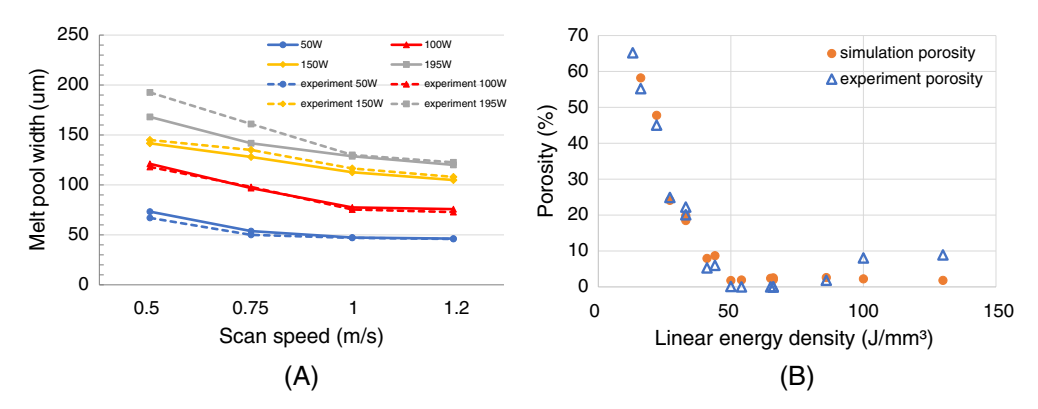


FIGURE 9 (A) Comparison between the calculated melt pool width for various laser powers and laser moving speeds for Ti6Al4V to experimental measurements; (B) Comparison of the predicted porosity for different volumetric energy density to the experimental characterization of the printed material Ti6Al4V [Color figure can be viewed at wileyonlinelibrary.com]

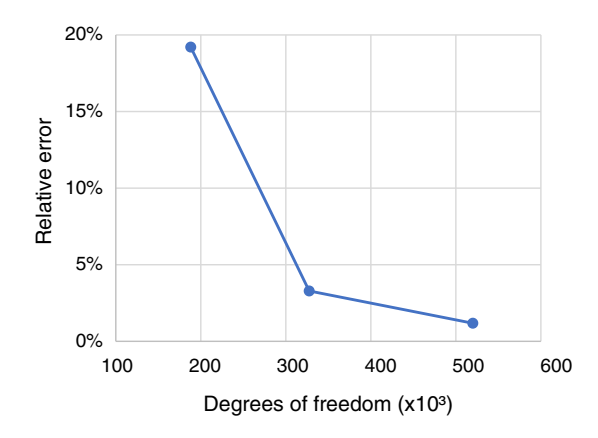


FIGURE 10 The relative error between the simulated melt pool width and experimental data converges to 0 as the number of degrees of freedom increases [Color figure can be viewed at wileyonlinelibrary.com]

Three initial meshes of the powder bed geometry are generated in addition to the mesh used above. The finest mesh has 519,920 degrees of freedom and 537,860 material points, and the coarsest mesh has 188,120 degrees of freedom and 177,480 material points. The relative error of the melt pool width measured from simulation results versus the number of degrees of freedom are shown in Figure 10. For the coarsest mesh, the relative error between the simulated melt pool width and experimental data is quite large. As the number of degrees of freedom in the geometry increased by a factor of two, the relative error of the simulated melt pool width drops from 19% to 3.3%. And the error further converges to 1.2% for the finest mesh. The convergence rate is estimated as around 2.

5 | NUMERICAL TESTS

After the validation of the HOTM method on the application of AM, in this section, we demonstrate the capability and efficiency of the proposed computational framework to investigate the correlation between the processing parameters and the microstructure of the printed material in PBF-based AM processes. The central processing parameters concerned in our simulations are the laser power and scanning speed, the number of layers of particles, and the packing density of the powder bed. The influence of processing parameters on the thermodynamics and dimensions of the melt pool, as well as defect formation, such as pores and unmelted or partially melted particles, is studied.

The simulations are mainly conducted for a multiple layer powder bed with a length of 1600 μ m and a width of 1200 μ m consisting of 744 spherical particles, as shown in Figure 11. The radii of the powder particles are ranged from 20 to 60 μ m following a Gaussian distribution centered at 40 μ m obtained from experimental measurements and shown in Figure 11A. The initial packing density of the powder bed is 55%, which gives us up

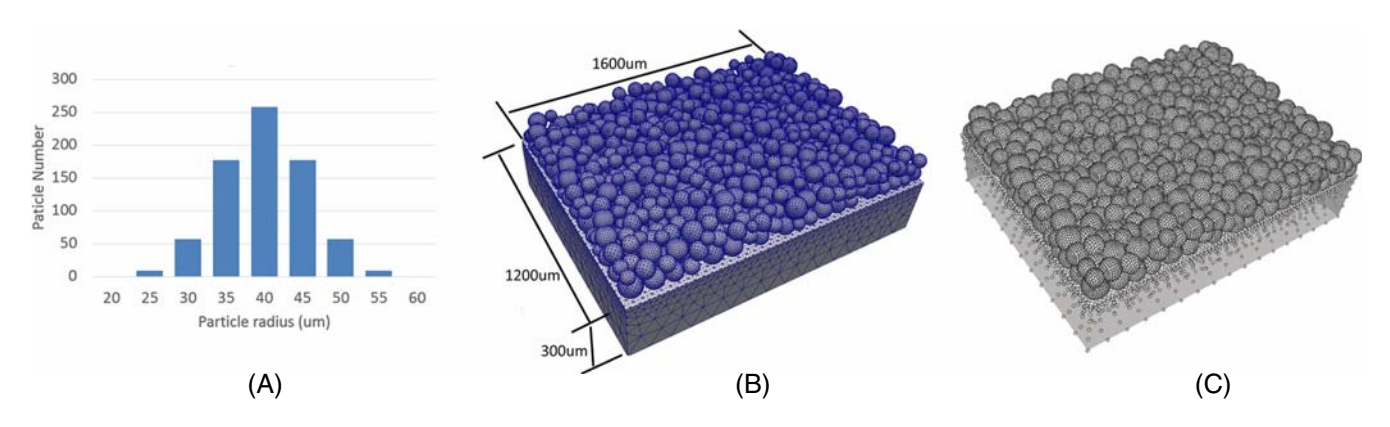


FIGURE 11 The powder bed geometry with given particle size distribution [Color figure can be viewed at wileyonlinelibrary.com]

FIGURE 12 (A) The profiles of the temperature dependent bulk modulus, shear modulus, and viscosity of aluminum. (B) The profiles of the temperature dependent heat conductivity and specific heat of aluminum [Color figure can be viewed at wileyonlinelibrary.com]

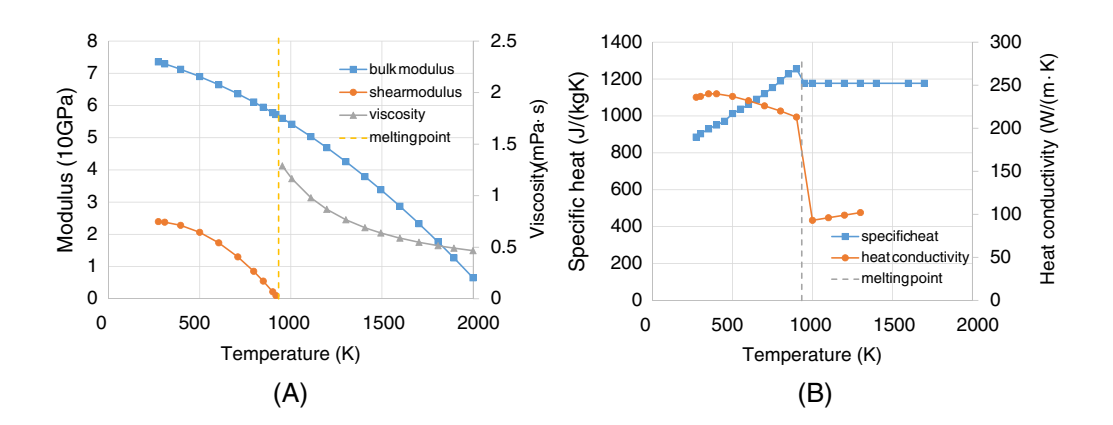


TABLE 2 Material properties of Al alloy

Density	Melting temperature	Latent heat of fusion	surface tension coefficient
$2700 (kg/m^3)$	933 (K)	396 (kJ/kg)	$0.86 (N/m)^{82}$

to three layers of particles in the thickness. The powder bed is placed on a substrate with a height of 300 μ m. As shown in Figure 11B, a tetrahedron mesh is created for the entire domain, including the powder particles and substrate, which results in 1,277,388 elements and 304,209 nodes. Barycenters of the elements are taken as the material points and vertices as the HOTM nodes, which leads to 1,277,388 material points and 304,209 degrees of freedom in Figure 11C. The initial connectivity of the tetrahedron mesh is utilized to construct the support of the HOTM nodes. However, the initial mesh is subsequently jettisoned, and the calculations proceed in a meshfree manner.

The material of the powder particles and the substrate is aluminum alloy 6061. The material properties required in the phase-aware thermomechanical constitutive model are obtained from the literature. Figure 12A shows the temperature dependent mechanical properties of the material, including the bulk modulus, ⁷⁸ shear modulus, ⁷⁸ and shear viscosity coefficient. ⁷⁹ The profiles of the heat conductivity ⁸⁰ and specific heat capacity of aluminum alloy as functions of temperature ⁸¹ are plotted in Figure 12B. The emissivity and convective heat conduction coefficient of the material are 0.1 and 100 W/(μ m²· K) as measured from experiments, respectively. A laser beam with a radius of 100 μ m is placed at the centerline of the powder bed and modeled as a Gaussian heat flux boundary condition. As suggested by King et al, ¹ the absorptivity coefficient in the Gaussian heat flux model ranges from 0.2 to 0.4 on the surfaces of the powder particles and the substrate depending on their interactions with the laser beam. The other material properties of the aluminum alloy are shown in Table 2. To this end, with the aid of the current setup, the influence of a variety of processing parameters, such as laser power and scanning speed, the powder bed packing density and thickness on the product quality is investigated in the following sections.

FIGURE 13 (A) The geometry of a powder bed with packing density of 55%; (B) The deformed configuration and temperature distribution in the cross-section of the powder bed predicted by the HOTM method at the end of the printing process with the laser power 300 W and scanning speed 1 m/s [Color figure can be viewed at wileyonlinelibrary.com]

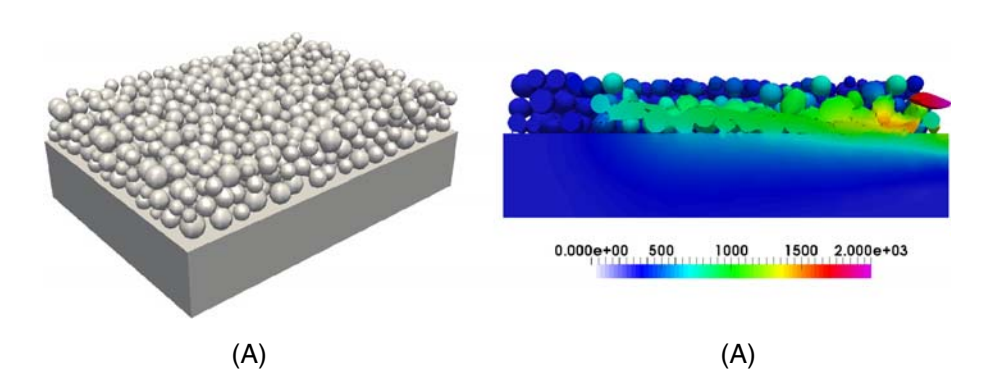


FIGURE 14 (A) The geometry of a powder bed with packing density of 40%; (B) The deformed configuration and temperature distribution in the cross-section of the powder bed at the end of the printing process with the laser power 300 W and scanning speed 1 m/s [Color figure can be viewed at wileyonlinelibrary.com]

5.1 | Powder bed configuration

To demonstrate the HOTM capability for simulating the dynamic contact of the AM PBF process, we first study the correlation between the configuration of the powder bed and the melt pool thermodynamics. In particular, the powder bed is characterized by the packing density and the number of layers of particles. Besides the aforementioned densely packed powder bed as shown in Figure 13A, a powder bed with a smaller packing density, 40%, is generated using the DEM method, as shown in Figure 14A. The loosely packed powder bed has the same number of particles and size distribution with the densely packed one. It is evident that there are more voids in the loosely packed powder bed, which mimics the situation of particles floating in space under the recoil pressure due to vaporization. These phenomena are commonly observed in experiments of PBF processes in which the densely packed powder bed is blown apart by the vapor before the laser beam arrives. It is called the denudation process of the powder bed and plays a significant role in the formation of the pores in the microstructure of the printed material. Thus, in the "in-situ" circumstances, it is a reasonable assumption that the packing density of a powder bed may be lower than its initial value.

The simulation result of the densely packed powder bed under the radiation of a 300 W laser beam traveling at 1 m/s is shown in Figure 13B. A continuous melt pool is formed and solidified, and only a few pores are formed. As indicated by the simulation results, particles under the laser radiation melt instantly, and the interaction between the melt pool and the powder bed becomes a FSI problem. For the powder particles away from the laser radiation, their temperature increase is small, and the recoil pressure is insignificant. Thus their deformation is in the regime of elastic deformation. Consequently, the effect of plasticity is negligible in the PBF process. The deformed powder bed with initial packing density of 40% under the same laser condition is illustrated in Figure 14B. Comparing to Figure 13B, the volume fraction of the partially melted particles increases drastically. More voids form in the printed material due to the low packing density. Figure 15 shows the detailed motion, deformation, and temperature evolution of the powder bed during the PBF process. As shown in Figure 15A,B, the particle highlighted in the circle on the powder bed surface is scanned by the laser beam and heated up via a heat conduction process from its surface to interior. The temperature rises immediately beyond the melting point and triggers the phase transition. Under the effect of recoil pressure, this fully melted particle or liquid droplet moves downwards and gets in touch with a small particle below, as shown in Figure 15C. The heat transfers from the melted particle to its neighbors in contact by heat conductivity. The small particle gets enough energy

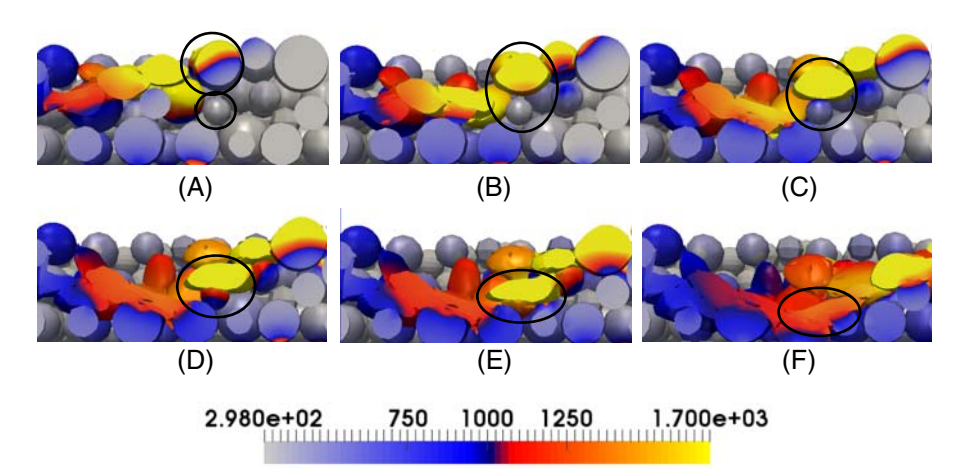
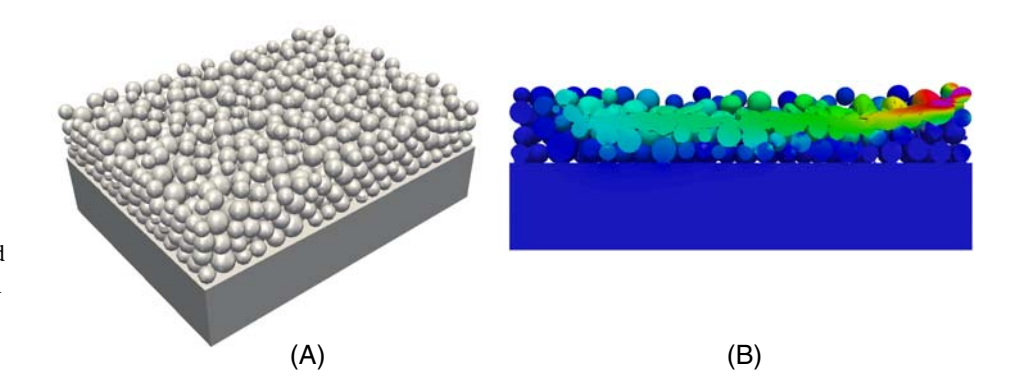


FIGURE 16 (A) The geometry of a powder bed with four layers of particles; (B) The deformed configuration and temperature distribution in the cross-section of the powder bed predicted by the HOTM method at the end of the printing process with the laser power 300 W and scanning speed 1 m/s [Color figure can be viewed at wileyonlinelibrary.com]



to activate the melting process and mixes with the liquid droplet, which is further compressed by the recoil pressure and moves down to meet the particles next to the substrate, as shown in Figure 15D,E. Finally, the solid, melted, or partially melted particles interact with each other by dynamic contact to create a complex melt pool. The dynamic contact process happens everywhere in the powder bed and underscores the fundamental mechanism of the melt pool formation. As the laser leaves the spot, the melt pool cools down and solidifies to finalize the microstructure of the printed layer. In this test, the low packing density leads to a low probability of dynamic contact and significantly reduces the effective heat conductivity of the powder bed. Thus, the particles at the bottom layers and the substrate may not receive enough energy to transit from solid to liquid phase. A particular type of defects, that is, a combination of partially melted particles and pores, can be easily found in PBF AM metals when denudation occurs.

Another powder bed geometry shown in Figure 16A consists of four layers and 816 particles, which follows the same size distribution in Figure 11A and with the packing density of 55%. As been recognized in previous studies, ^{1,77} the number of layers of powder particles employed for the print of one slice must be carefully picked, which is supposed to be dependent on the raw material, the size of the particles, and laser properties. The influence of the number of powder bed layers on the quality of the printed slice under laser power of 300 W at 1 m/s scanning speed is studied by the HOTM simulations. The predicted deformed configuration and temperature distribution in the powder bed are shown in Figure 16B. It can be noticed that the laser power only melts the top two layers of particles. The temperature in the vicinity of the substrate remains low, and no melt pool at the substrate is formed. Thus, a thick powder bed is not practical for this specific laser power and travel speed, which may induce a non-fused slice of materials. Again, the extremely large deformation, motion, and dynamic contact of the particles at various phases, and the mixing of the liquid droplets postulate grand challenges to conventional Eulerian methods and grid-based Lagrangian methods. However, high-fidelity and high-resolution predictions of the strongly coupled thermal-fluid-structure interactions (TFSI) during the PBF AM processes are enabled in the HOTM simulations at the powder scale. It is noteworthy that the direct mesoscale simulation of the powder bed based on the HOTM method furnishes a robust and efficient means of quantifying the correlation between a diversity of processing parameters and the material defects on the mesoscale of the printed material. It also sheds light on the fundamental understanding of the strongly coupled multiphysics during the PBF AM processes.

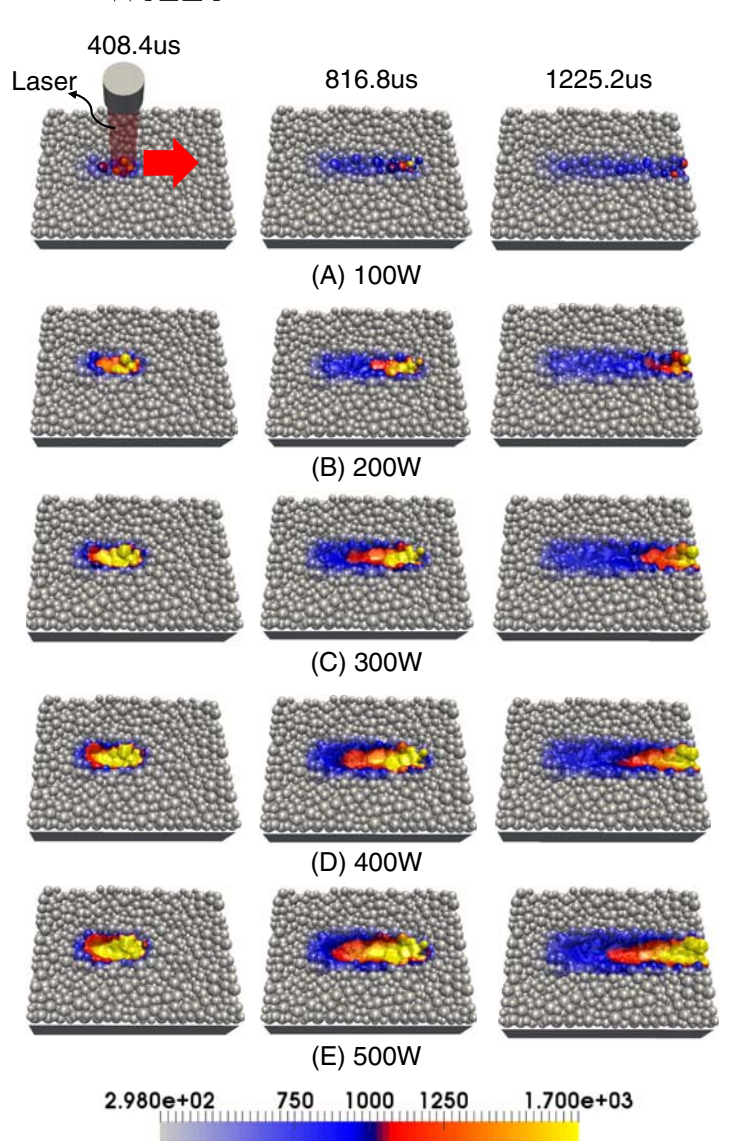


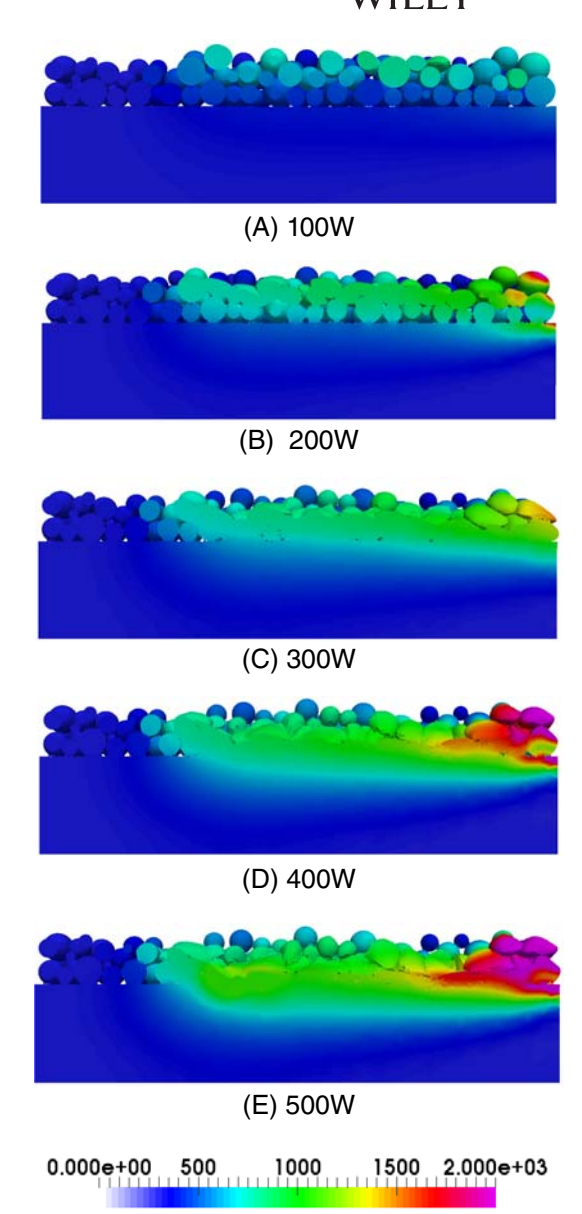
FIGURE 17 The simulation result of the PBF process for laser speed 1 m/s and power varying from 100 to 500 W. The color indicates the temperature (K). (A) 100 W. (B) 200 W. (C) 300 W. (D) 400 W. (E) 500 W [Color figure can be viewed at wileyonlinelibrary.com]

5.2 | Laser power

The HOTM simulation results of the PBF AM processes for the laser scanning speed of 1 m/s are shown in Figure 17. We consider five different cases using the laser power from 100 to 500 W. Figures 17 and 18 illustrate the temperature evolution in the powder bed and the cross-section of the deformed configuration of the melt pool at 123 μ s, respectively. As observed in Figure 17, the melting of powder particles becomes significant, and the deformation of the melt pool is more excessive when the laser power increases. Particularly, the laser power of 100 W in Figure 17A can barely form a melt pool in the powder bed and fails to print a solid part from discrete particles. Under the laser power of 500 W in Figure 17E, a wide and deep melt pool is created due to heat conduction and recoil pressure.

The formation mechanism of the melt pool and thermomechanical responses of the powder bed are made clear in the cross-section snapshots of the domain in Figure 18. With the aid of the direct numerical simulation (DNS) based on the HOTM method, a detailed description of the temperature and phase evolution in the particles is obtained. As the laser beam scans over the surface of the powder bed, particles at the top layer absorb most of the laser energy, and the applied heat flux starts to heat individual particles. When the local temperature at a material point reaches the melting temperature, the material point transits to the fluid phase. If the laser power is intensive, the entire particle may melt after the heat transfers from the heat flux boundary to the interior. Otherwise, it remains as solid or partially melted. Particles at the lower layers are also scanned by the laser beam due to the porosity of the powder bed. However, since the boundary of the lower particles is partially radiated by the laser, the temperature rise is limited in these particles as well as the

FIGURE 18 The cross sections of simulation results at the end of the printing process for laser speed 1 m/s and power varying from 100 to 500 W. The color indicates the temperature (K). (A) 100 W. (B) 200 W. (C) 300 W. (D) 400 W. (E) 500 W [Color figure can be viewed at wileyonlinelibrary.com]



substrate. Besides, recoil pressure is applied to those nodes on the free surfaces whose temperature is beyond the melting temperature, which combines with the gravity and surface tension to drive the particles to move and deform. Melted or partially melted particles spread out and are squeezed into the pores of the powder bed under the external forces leading to extensive dynamic contact between different layers. As a consequence of the enhanced contact area, heat transfer from the particles at the top layers to the bottom layers is much promoted, which further raises the temperature of the particles at lower layers and the substrate and may cause them to melt as well.

As shown in Figure 18A,B, the internal particles and the substrate do not melt not only due to the low energy density absorbed directly from the laser but also the deficient dynamic contacts in the loosely packed powder bed resulting from a low temperature-dependent recoil pressure. As the laser beam travels away, the heat is dissipated to the environment by convective heat conduction and radiation, which are also modeled as heat flux boundary conditions in the HOTM simulations. Thus, the melt pool cools down to create a solid part. However, in Figure 18A,B, no continuous material system is fabricated, and a significant amount of voids form in the final product. Eventually, the quality of the fabricated material under laser power of 100 and 200 W is very low owing to the weak bond of the particles and significant porosity in the microstructure, which may result in low stiffness and fracture toughness.

We increase the laser power to 300 W in Figure 18C. The top layer's temperature rises quickly beyond the melting point, which yields high recoil pressure on the free surface. The dynamic contact between particles and the melt pool driven by the recoil pressure becomes aggressive. The pressure boundary condition facilitates the fluid flow of the melted

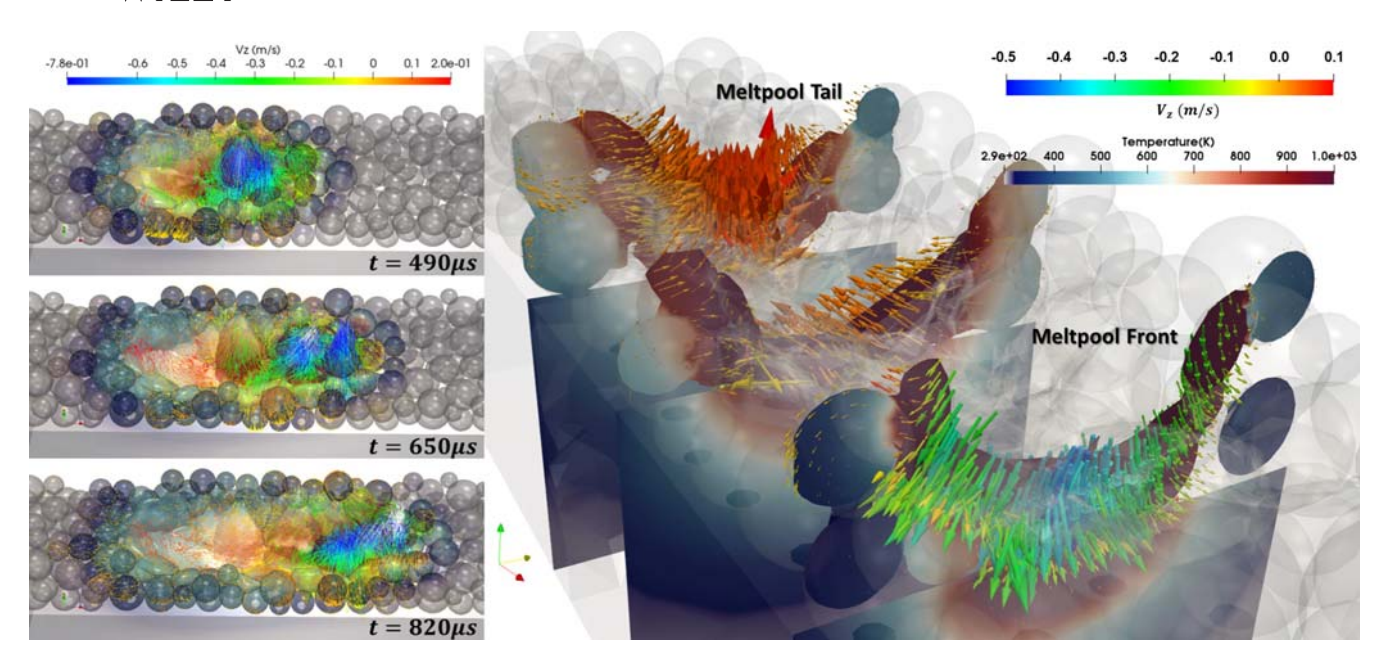


FIGURE 19 The velocity field in the meltpool at laser power of 300 W and scanning speed of 1 m/s: (Left) time evolution of the velocity field where the color shows the speed of nodes in the normal direction of the powder bed; (Right) snapshot of the velocity field at $t = 820 \,\mu\text{s}$ [Color figure can be viewed at wileyonlinelibrary.com]

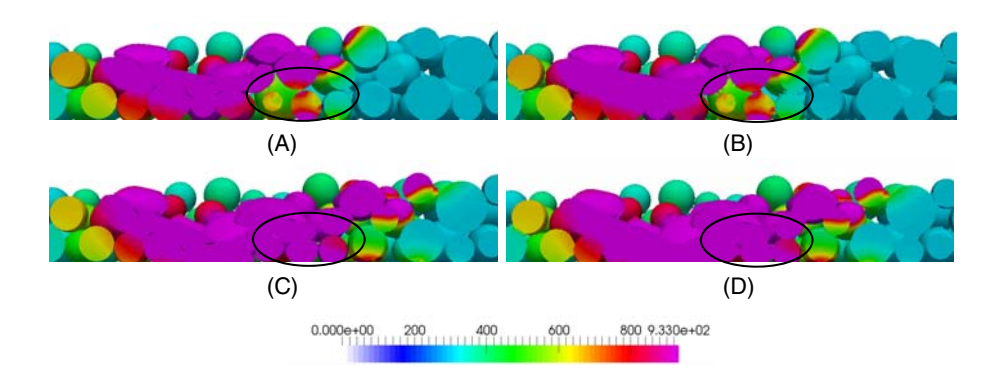


FIGURE 20 The dynamic contact between particles and the absorption of the melted particles to the melt pool. The color indicates the temperature (K) [Color figure can be viewed at wileyonlinelibrary.com]

or partially melted particles. Figure 19 displays the velocity field and mass transport profile at three cross-sections of the melt pool. The front of the melt pool is highly compressed due to the excessive pressure of vaporized material. The liquid metal flows towards the substrate at an average velocity of 0.4 m/s and pushes the neighboring particles away from the melt pool. At the mid-section, the melt pool cools down, and the recoil pressure drops. The liquid metal travels horizontally to the back of the melt pool due to the mass transport from the laser front, and downward mass flow is not evident. While the material accumulates at the tail-section, an upward motion at a maximum velocity of 0.2 m/s is observed in the melt pool due to the surface tension and conservation properties. It is noteworthy that the neighboring particles are dragged into the melt pool at the mid- and tail-section, as indicated by the velocity field. Phase transition of the lower layers and substrate is noticeable because of the intensive FSI and heat conduction between different layers. Figure 20 shows the time evolution of the predicted melt pool. As highlighted, the particle next to the substrate is heated up from two directions simultaneously through dynamic contact with a melted particle on top and the substrate at the bottom. While it melts, the particle is compressed by the top particle in contact and absorbed by the melt pool on the substrate gradually. Neighboring liquid particles spread flat under the contact forces and flow to fill the gap in the powder bed. When the liquid particles meet, they are well mixed, and the melt pool forms and grows. This phenomenon is extensively observed in experiments by X-ray technology. 14,16,18 However, porosity at the interface of particles and the substrate can be found, resulting from the unmelted or partially melted particles in the melt pool. Overall, the quality of the printed material is not desirable using the laser power of 300 W for the given powder bed.

In Figure 18D,E, the laser power is further increased to 400 and 500 W. The dynamic contact further intensifies. It is evident that the liquid particles and the melted substrate material are well mixed in the melt pool, and a dense solid part is generated as one layer of the final product. Thus, the product quality may be improved as the laser power increases. This trend is consistent with experimental observations. It is worth mentioning that the mixing of the melted particles and the substrate, as well as the interaction between the melt pool and unmelted or partially melted particles are key factors to the product quality. Overall, this process is determined by the strongly coupled multiphysics, involving large deformation, transient heat transfer, phase transition, free surface boundary conditions, dynamic contact, and FSI, which further relies on the applied laser power. Most of the numerical studies based on Eulerian methods simplify or even neglect the particle-particle/particle-substrate dynamic contact and FSIs in the powder bed. However, high fidelity predictions of the material defects formation on the mesoscale in the printed material must account for the discrete and granular nature of the powder bed, which is the major strength of the proposed direct mesoscale simulation capability based on the HOTM method. Instead of introducing an effective thermal conductivity model that addresses four of the main thermal transport phenomena in the powder bed: thermal conductivity of contact between particles, vapor thermal conductivity, thermal radiation, thermal conductivity of an individual particle, the DNS based on the HOTM method models all these phenomena explicitly in the aggregation of discrete powder particles. It can also be utilized to verify the empirical effective thermal conductivity models.

5.3 | Laser scanning speed

The influence of varying laser scanning speed on the PBF process is also investigated in this work. Figure 21 shows the comparison of the predicted melt pool by the HOTM simulations for two different scanning speeds of 2 and 0.5 m/s with a laser power of 300 W for the densely packed powder bed. The cross-section of the melt pool at the end of the printing process is demonstrated in Figure 21B,D. It can be observed in the simulation results that the width and depth of the melt pool increase as the speed decreases. In Figure 21A,B, the laser beam travels so fast that the powder bed has limited time to absorb the laser energy and only particles at the top layer melt. The melt pool fails to solidify into a continuous solid part. Comparing to Figures 17C and 18C, as the laser beam slows down to 0.5 m/s, the temperature of particles under radiation increases, which leads to intensified recoil pressure and dynamic contact between particles. Therefore, the heat transfer between the powder bed and melt pool increases and voids at the interface of the powder bed and the substrate caused by the partially melted particles disappear in the material as shown in Figure 21D. Thus, for these three cases at a laser power of 300 W, it may be concluded that the product quality is enhanced by decreasing the laser scanning speed or increasing the linear energy density (i.e., laser power/scanning speed) since there are fewer voids form in the microstructure. Nevertheless, there is a critical energy density beyond which the metallurgical pores may form. In this case, the high energy density causes intensive vaporization of the material in the powder bed and results in huge recoil pressure. The pressure applied to the free surface of the melt pool generates deep penetration in the substrate. As the

FIGURE 21 The comparison of simulation results of different laser speeds with laser power 300 W. (B) and (D) shows the corresponding cross sections at the end of the printing process. The color indicates the temperature (K) [Color figure can be viewed at wileyonlinelibrary.com]

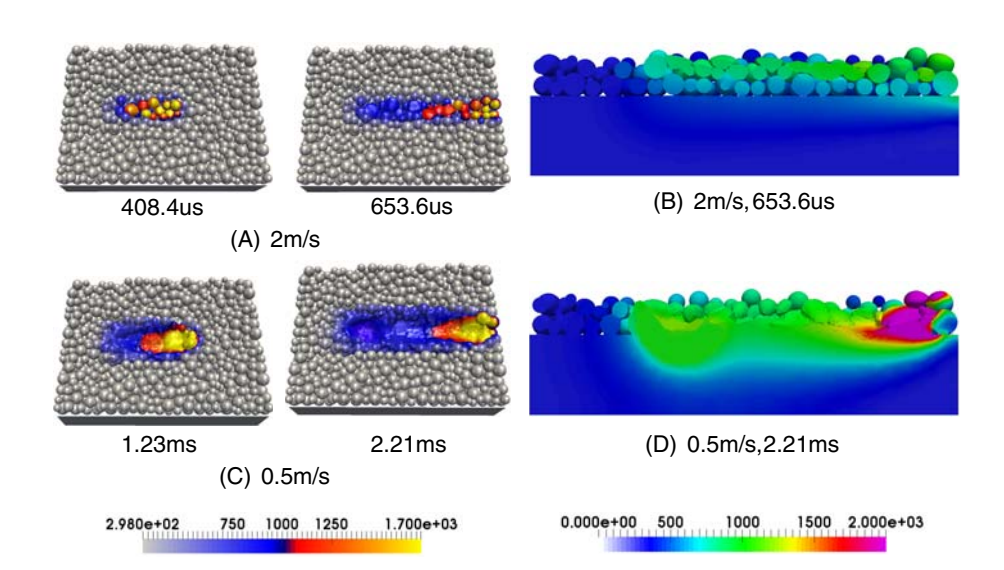


TABLE 3 Simulation results summary

Laser speed (m/s)	Laser power (W)	Energy density (J/mm³)	Melt pool width (μm)	Melted particle ratio	Porosity
0.5	100	12.5	159.20	27.59%	23.79%
	200	25	240.08	86.21%	2.85%
	300	37.5	281.89	100%	1.44%
	400	50	252.36	100%	1.11%
	500	62.5	400.00	100%	0.66%
1	100	6.25	109.22	4.31%	43.00%
	200	12.5	160.39	28.44%	23.13%
	300	18.75	203.72	74.13%	5.46%
	400	25	250.30	86.21%	2.24%
	500	31.25	270.43	100%	1.51%
2	100	3.125	N/A	0.00%	43.00%
	200	6.25	121.26	7.76%	36.59%
	300	9.375	157.10	17.24%	33.08%
	400	12.5	169.90	28.45%	29.88%
	500	15.625	194.43	38.79%	12.00%

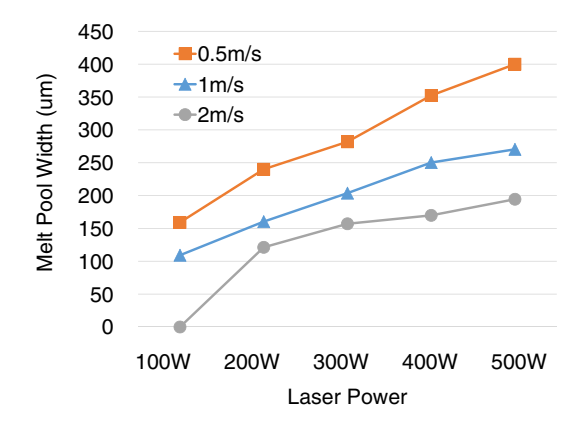


FIGURE 22 The simulated melt pool width for different laser powers and laser moving speeds [Color figure can be viewed at wileyonlinelibrary.com]

laser moves away, the vapor may be trapped in the substrate to form a small size spherical void. The metallurgical pores formation mechanism is not observed in the range of our simulated energy density.

The direct mesoscale simulation results for the given powder bed with an initial packing density of 55% are summarized in Table 3.

The geometric dimensions of the melt pool, the volume fraction of fully melted particles in the laser scanning region, and the porosity of the laser melt track are concerned as the metrics of the performance measurement for the PBF AM processes. In specific, they are dependent on the laser power and scanning speed, which is plotted in Figures 22 to 24. In Figure 22, it is readily shown that the average melt pool width increases monotonically as the laser power increases, and the laser scanning speed reduces. Melting of the powder particles at low scanning speed is greatly promoted following a power-law function of the laser power, while the volume fraction of the fully melted particles increases linearly at the scanning speed of 2 m/s as we raise the laser power, as shown in Figure 23. Notably, all the particles may melt under a relatively low laser power, as indicated by the plot of laser speed of 0.5 m/s. The porosity of the final product versus the VED,⁷⁷ which is an indicator of the product quality, is illustrated in Figure 24. It is evident that the predicted porosity of the printed material Al6061 is in a good agreement with the experimental measurements in Reference 83.

FIGURE 23 The simulated melted particles ratio for different laser powers and laser moving speeds [Color figure can be viewed at wileyonlinelibrary.com]

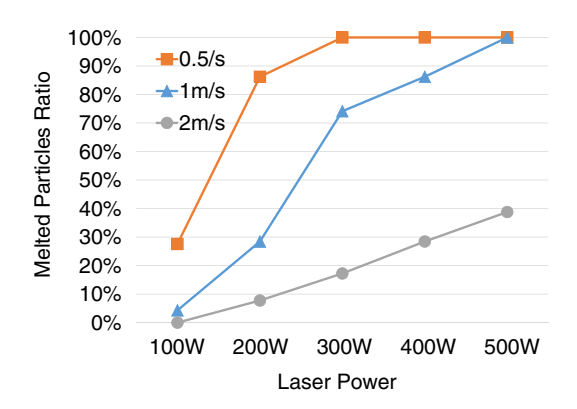
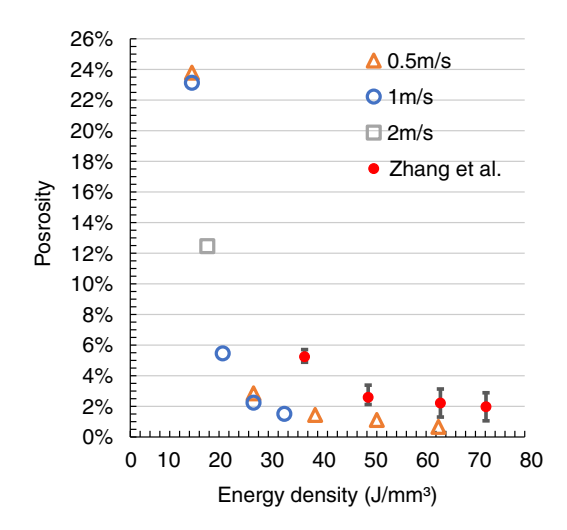


FIGURE 24 The simulated porosity for different energy densities⁸³ [Color figure can be viewed at wileyonlinelibrary.com]



6 | CONCLUSION

In this work, we developed an incremental updated Lagrangian computational framework for the DNS of PBF based AM of metals at the powder-scale based on the HOTM method. In specific, a geometric modeling approach is presented by employing the DEM to create a realistic powder bed as an aggregation of discrete particles in solids. The statistical information of the powder bed, including particle size and shape distribution, particle material properties, as well as powder bed packing density, measured from experiments, can be readily integrated into the computational model. Low-quality particles, such as hollow spheres and second phase inclusions, can be modeled explicitly as well in this method. Besides, a phase-aware constitutive relation is developed within the variational constitutive update framework to describe the thermo-visco-elastic response of the metallic particles in PBF processes involving the melting/solidification phase transition. The particle-particle and particle-substrate interactions in various phases are simulated using the OTM contact algorithm for a detailed description of the dynamic contact between solids, FSI, and liquid particles and substrate mixing. Furthermore, a nodal integration scheme for the surface integrals in the meshfree setting is proposed to model the realistic boundary conditions of the PBF processes on the free surfaces of the powder bed, such as the laser power, recoil pressure, and surface tension, instead of approximating them as heat sources and body forces, respectively. To this end, the discrete system of equations, including the linear momentum and energy conservation equations of the powder bed is solved simultaneously in a meshfree manner within the incremental update Lagrangian framework to predict the deformation, motion, temperature, and phase evolution of the domain. The proposed HOTM method is validated by comparing the melt pool width and product porosity measured from simulation results and experimental results of Dilip et al⁴⁷ for a single-layer powder bed. The prediction of the HOTM method agrees very well with experimental observations. Finally, we investigated the correlation between the processing parameters and the quality of the printed materials by adopting the HOTM framework for a realistic multi-layer powder bed. The influence of the powder bed characteristics, laser power, and laser scanning speed on the melt pool dimensions and the defect formation in the microstructure of printed materials is quantified by conducting a series of DNS of the PBF AM processes.

Our simulation results show that the average melt pool width increases monotonically as the laser power increases, and the laser scanning speed reduces. Melting of the powder particles is significantly promoted, and the formation of pores is suppressed at low laser scanning speed or higher laser power. It can be concluded that the quality of the printed material by the PBF AM process may be enhanced by increasing the VED. However, beyond a critical value of the VED, this trend may reverse due to the keyhole mode. On the other hand, the powder bed configuration plays a vital role in controlling the quality of printed materials. A thick powder bed with multiple layers of particles may end with many nonfused particles near the substrate when processed by a moderate laser. As the particles are blown apart by the vapor, the powder bed becomes loosely packed, which results in more space for the particles to travel and a low probability of dynamic contact with neighbors. A higher volume fraction of unmelted or partially melted particles can be observed in this situation.

Overall, the powder particles experience a complex thermomechanical history during the PBF process. As a high energy density pulse applied to the surface of the powder bed, phase transition, such as melting and vaporization of the particles, can take place very quickly, arising from the heat conduction from the free surface to the interior of the material at a very high heating rate. Their temperature and phase evolution is determined by the particle material properties and size, the laser power and scanning speed, as well as the hatching space. In the meantime, the vaporized particles generate a recoil pressure on the powder bed. Since the powder bed is a discrete system, particles move under the recoil pressure and gravity to meet the neighbors. Dynamic contact in this multibody system activates heat transfer, deformation, and motion of the powder bed. Various types of contact mechanisms can be found in the powder bed, including solid-solid contact, FSI, and mixing of liquid particles and the substrate material. The movement of individual particles and the probability of dynamic contact with neighbors are constrained by the powder bed configuration, such as the packing density and powder bed thickness, as well as their kinetic energy due to the work of external forces. It is noteworthy that no evident plasticity is found in the PBF process. Therefore conventional stress models that neglect the plastic effect of materials can be employed to predict the PBF process. It is evident that the strongly coupled thermal-FSIs and dynamic contact in the PBF AM process underscore the formation mechanism and thermodynamics of the melt pool. By modeling the powder bed explicitly as an aggregation of discrete particles under thermomechanical boundary conditions, the proposed DNS based on the HOTM method enables a high-fidelity prediction of PBF AM processes at the mesoscopic scale and furnishes an effective means of quantifying the sensitivity of the quality of the printed materials on the processing parameters.

Nevertheless, there are a few limitations in a Lagrangian meshfree framework. First of all, the lack of a surface representation in meshfree methods limits the accurate modeling of the Neumann boundary conditions. Although a nodal integration scheme is adopted to calculate the surface tension and recoil pressure on the free surfaces of the powder bed in our framework, the accuracy and stability of the solution necessitate a very fine discretization of the surfaces. Moreover, the OTM seizing-contact algorithm allows for mixing of materials. Thus it is a challenge to maintain the nonpenetration condition during the dynamic contact of particles and the substrate. The contact algorithm also prohibits sliding between particles causing unrealistic frictional forces during solid-liquid interaction and solid-solid contact. To stabilize the meshfree simulations, a Lagrangian artificial viscosity model is employed. The artificial viscosity coefficients are found by numerical experiments. But to complete the simulation of the printing process, large artificial viscosity needs to be added to the material leading to a highly viscous flow. In addition, the nearly incompressibility of the liquid state of the material constrains the flow of the melt pool. And the lack of an accurate way to show the meshfree solutions by volume can further contribute to an unrealistic representation of the melt pool. Finally, the FSI between the solid and melted material is solved using the monolithic meshfree solution. The internal material interface is presented by nodes belonging to the influence domain of material points in solid and liquid phases. Thus, no sharp material interface is explicitly modeled in our simulations but a zone of interfacial nodes. These challenges are also recognized in other numerical methods for the modeling of the PBF AM processes, such as the Eulerian method with the VOF approach. Further studies of the influences of the mixing of multiphase interfaces on the accuracy of the final results are necessary. Several other effects in the PBF AM process, such as the Marangoni convection due to temperature-dependent surface tension, wetting forces at the triple line solid melt-gas, and the fluid and phase change dynamics in the surrounding gas phase, are not considered in the present model.

ACKNOWLEDGEMENTS

The authors are grateful for the support from the National Science Foundation under Grant Number CMMI-1652839. This work made use of the High Performance Computing Resource in the Core Facility for Advanced Research Computing at Case Western Reserve University.

ORCID

Huming Liao https://orcid.org/0000-0003-1697-9148 *Bo Li* https://orcid.org/0000-0002-0127-8210

REFERENCES

- 1. King WE, Anderson AT, Ferencz RM, et al. Laser powder bed fusion additive manufacturing of metals; physics, computational, and materials challenges. *Appl Phys Rev.* 2015;2(4):041304.
- National Science and Technology Council: Committee on Technology (CoT), Interagency working group on Advanced Manufacturing (IAM). "A National Strategic Plan for Advanced Manufacturing", Executive Office of the President of the United States, Washington, DC, February 2012.
- 3. U.S. Congress, House Committee on Science, Space, and Technology, Subcommittee on Technology and Innovation. Assembling the Facts: Examining the Proposed National Network for Manufacturing Innovation, 112th Congress 2nd session, U.S. National Institute of Standards and Technology, May 31, 2012.
- 4. President's Council of Advisors on Science and Technology. Report to the President on Ensuring American Leadership in Advanced Manufacturing, Executive Office of the President of the United States Washington, DC, June 2011. http://www.whitehouse.gov/sites/default/files/microsites/ostp/pcast-advanced-manufacturing-june2011.pdf.
- 5. Wohlers T. US Manufacturing Competitiveness Initiative Dialogue. Oak Ridge, TN: Council on Competitiveness; 2013.
- 6. Olson GB. Computational design of hierarchically structured materials. Science. 1997;277(5330):1237-1242.
- 7. Kamath C, El-dasher B, Gallegos GF, King WE, Sisto A. Density of additively-manufactured, 316l ss parts using laser powder-bed fusion at powers up to 400 w. *Int J Adv Manuf Technol*. 2014;74(1-4):65-78.
- 8. Kempen K, Vrancken B, Buls S, Thijs L, Van Humbeeck J, Kruth J-P. Selective laser melting of crack-free high density m2 high speed steel parts by baseplate preheating. *J Manuf Sci Eng.* 2014;136(6):061026.
- 9. Scipioni Bertoli U, Wolfer AJ, Matthews MJ, Delplanque J-PR, Schoenung JM. On the limitations of volumetric energy density as a design parameter for selective laser melting. *Mater Des.* 2017;113:331-340.
- 10. Gong H, Rafi K, Gu H, Starr T, Stucker B. Analysis of defect generation in ti-6al-4v parts made using powder bed fusion additive manufacturing processes. *Addit Manuf*. 2014;1:87-98.
- 11. Kruth JP, Badrossamay M, Yasa E, et al. Part and material properties in selective laser melting of metals. Paper presented at: Proceedings of the 16th International Symposium on Electromachining; vol. 16. Shanghai Jiao Tong Univ Press; 2010:3-14.
- 12. Cunningham R, Narra SP, Montgomery C, Beuth J, Rollett AD. Synchrotron-based x-ray microtomography characterization of the effect of processing variables on porosity formation in laser power-bed additive manufacturing of ti-6al-4v. *JOM*. 2017;69(3):479-484.
- 13. Bidare P, Bitharas I, Ward RM, Attallah MM, Moore AJ. Fluid and particle dynamics in laser powder bed fusion. *Acta Mater*. 2018;142:107-120.
- 14. Guo Q, Zhao C, Escano LI, et al. Transient dynamics of powder spattering in laser powder bed fusion additive manufacturing process revealed by in-situ high-speed high-energy x-ray imaging. *Acta Mater*. 2018;151:169-180.
- 15. Zhao C, Fezzaa K, Cunningham RW, et al. Real-time monitoring of laser powder bed fusion process using high-speed x-ray imaging and diffraction. *Sci Rep.* 2017;7(1):3602.
- 16. Parab ND, Zhao C, Cunningham R, et al. Ultrafast x-ray imaging of laser–metal additive manufacturing processes. *J Synchrotron Radiat*. 2018;25(5):1467-1477.
- 17. Lu Y, Wu S, Gan Y, et al. Study on the microstructure, mechanical property and residual stress of slm inconel-718 alloy manufactured by differing island scanning strategy. *Opt Laser Technol.* 2015;75:197-206.
- 18. Scipioni Bertoli U, Guss G, Wu S, Matthews MJ, Schoenung JM. In-situ characterization of laser-powder interaction and cooling rates through high-speed imaging of powder bed fusion additive manufacturing. *Mater Des.* 2017;135:385-396.
- 19. Yadroitsev I, Bertrand P, Smurov I. Parametric analysis of the selective laser melting process. Appl Surf Sci. 2007;253(19):8064-8069.
- 20. Mozaffar M, Ndip-Agbor E, Lin S, Wagner GJ, Ehmann K, Cao J. Acceleration strategies for explicit finite element analysis of metal powder-based additive manufacturing processes using graphical processing units. *Comput Mech.* 2019;64(3):879-894.
- 21. Cheng B, Price S, Lydon J, Cooper K, Chou K. On process temperature in powder-bed electron beam additive manufacturing: model development and validation. *J Manuf Sci Eng.* 2014;136(6):061018.
- 22. Price S, Cheng B, Lydon J, Cooper K, Chou K. On process temperature in powder-bed electron beam additive manufacturing: process parameter effects. *J Manuf Sci Eng.* 2014;136(6):061019.
- 23. Rauniyar SK, Chou K. Melt pool analysis and mesoscale simulation of laser powder bed fusion process (l-pbf) with ti-6al-4v powder particles. *JOM*. 2019;71(3):938-945.
- 24. Dai D, Gu D. Thermal behavior and densification mechanism during selective laser melting of copper matrix composites: simulation and experiments. *Mater Des.* 2014;55:482-491.
- 25. Yuan P, Gu D. Molten pool behaviour and its physical mechanism during selective laser melting of tic/alsi10mg nanocomposites: simulation and experiments. *J Phys D Appl Phys.* 2015;48(3):035303.
- 26. Dai D, Gu D. Tailoring surface quality through mass and momentum transfer modeling using a volume of fluid method in selective laser melting of tic/alsi10mg powder. *Int J Mach Tools Manuf*. 2015;88:95-107.
- 27. Yan W, Ge W, Qian Y, et al. Multi-physics modeling of single/multiple-track defect mechanisms in electron beam selective melting. *Acta Mater.* 2017;134:324-333.

- 28. Gürtler F-J, Karg M, Leitz K-H, Schmidt M. Simulation of laser beam melting of steel powders using the three-dimensional volume of fluid method. *Phys Proc.* 2013;41:881-886.
- 29. Yan W, Qian Y, Ge W, et al. Meso-scale modeling of multiple-layer fabrication process in selective electron beam melting: inter-layer/track voids formation. *Mater Des.* 2018;141:210-219.
- Khairallah SA, Anderson A. Mesoscopic simulation model of selective laser melting of stainless steel powder. J Mater Process Technol. 2014;214(11):2627-2636.
- 31. Khairallah SA, Anderson AT, Rubenchik A, King WE. Laser powder-bed fusion additive manufacturing: physics of complex melt flow and formation mechanisms of pores, spatter, and denudation zones. *Acta Mater.* 2016;108:36-45.
- 32. Matthews MJ, Guss G, Khairallah SA, Rubenchik AM, Depond PJ, King WE. Denudation of metal powder layers in laser powder bed fusion processes. *Acta Mater*. 2016;114:33-42.
- 33. Attar E, Körner C. Lattice Boltzmann model for thermal free surface flows with liquid–solid phase transition. *Int J Heat Fluid Flow*. 2011;32(1):156-163.
- 34. Bauereiß A, Scharowsky T, Körner C. Defect generation and propagation mechanism during additive manufacturing by selective beam melting. *J Mater Process Technol.* 2014;214(11):2522-2528.
- 35. Klassen A, Scharowsky T, Körner C. Evaporation model for beam based additive manufacturing using free surface lattice Boltzmann methods. *J Phys D Appl Phys.* 2014;47(27):275303.
- 36. Markl M, Ammer R, Rüde U, Körner C. Numerical investigations on hatching process strategies for powder-bed-based additive manufacturing using an electron beam. *Int J Adv Manuf Technol*. 2015;78(1-4):239-247.
- 37. Hodge NE, Ferencz RM, Solberg JM. Implementation of a thermomechanical model for the simulation of selective laser melting. *Comput Mech.* 2014;54(1):33-51.
- 38. Riedlbauer D, Scharowsky T, Singer RF, Steinmann P, Körner C, Mergheim J. Macroscopic simulation and experimental measurement of melt pool characteristics in selective electron beam melting of ti-6al-4v. *Int J Adv Manuf Technol.* 2017;88(5-8):1309-1317.
- 39. Gusarov AV, Yadroitsev I, Bertrand P, Smurov I. Heat transfer modelling and stability analysis of selective laser melting. *Appl Surf Sci.* 2007;254(4):975-979.
- 40. Pal D, Patil N, Zeng K, Stucker B. An integrated approach to additive manufacturing simulations using physics based coupled multiscale process modeling. *J Manuf Sci Eng.* 2014;136(6):061022.
- 41. Fan Z, Li B. Meshfree simulations for additive manufacturing process of metals. Integr Mater Manuf Innov. 2019;8(2):144-153.
- 42. Gu D, Xia M, Dai D. On the role of powder flow behavior in fluid thermodynamics and laser processability of ni-based composites by selective laser melting. *Int J Mach Tools Manuf*. 2019;137:67-78.
- 43. Wang H, Liao H, Fan Z, et al. The hot optimal transportation meshfree (hotm) method for materials under extreme dynamic thermomechanical conditions. *Comput Methods Appl Mech Eng.* 2020;112958(06):364.
- 44. Li B, Habbal F, Ortiz M. Optimal transportation meshfree approximation schemes for fluid and plastic flows. *Int J Numer Methods Eng.* 2010;83(12):1541-1579.
- 45. Yang Q, Stainier L, Ortiz M. A variational formulation of the coupled thermo-mechanical boundary-value problem for general dissipative solids. *J Mech Phys Solids*. 2006;54(2):401-424.
- 46. Stainier L. A variational approach to modeling coupled thermo-mechanical nonlinear dissipative behaviors. *Advances in Applied Mechanics*. Vol 46. San Diego, CA: Academic Press; 2013:69-126.
- 47. Dilip JJS, Zhang S, Teng C, et al. Influence of processing parameters on the evolution of melt pool, porosity, and microstructures in ti-6al-4v alloy parts fabricated by selective laser melting. *Progr Addit Manuf*. 2017;2(3):157-167.
- 48. Chen H, Wei Q, Wen S, Li Z, Shi Y. Flow behavior of powder particles in layering process of selective laser melting: numerical modeling and experimental verification based on discrete element method. *Int J Mach Tools Manuf*. 2017;123:146-159.
- 49. Haeri S. Optimisation of blade type spreaders for powder bed preparation in additive manufacturing using dem simulations. *Powder Technol.* 2017;321:94-104.
- 50. Han Q, Gu H, Setchi R. Discrete element simulation of powder layer thickness in laser additive manufacturing. *Powder Technol*. 2019;352:91-102.
- 51. Meier C, Weissbach R, Weinberg J, Wall WA, Hart AJ. Critical influences of particle size and adhesion on the powder layer uniformity in metal additive manufacturing. *J Mater Process Technol.* 2019;266:484-501.
- 52. Meier C, Weissbach R, Weinberg J, Wall WA, John Hart A. Modeling and characterization of cohesion in fine metal powders with a focus on additive manufacturing process simulations. *Powder Technol.* 2019;343:855-866.
- 53. Nan W, Ghadiri M. Numerical simulation of powder flow during spreading in additive manufacturing. Powder Technol. 2019;342:801-807.
- 54. Chen H, Wei Q, Zhang Y, Chen F, Shi Y, Yan W. Powder-spreading mechanisms in powder-bed-based additive manufacturing: experiments and computational modeling. *Acta Mater*. 2019;179:158-171.
- 55. Gottschalk S, Lin MC, Manocha D. Obbtree: a hierarchical structure for rapid interference detection. Paper presented at: Proceedings of the 23rd Annual Conference on Computer Graphics and Interactive Techniques. New Orleans, Louisiana; 1996:171-180.
- 56. Kruggel-Emden H, Simsek E, Rickelt S, Wirtz S, Scherer V. Review and extension of normal force models for the discrete element method. *Powder Technol.* 2007;171(3):157-173.
- 57. Steuben JC, Iliopoulos AP, Michopoulos JG. Discrete element modeling of particle-based additive manufacturing processes. *Comput Methods Appl Mech Eng.* 2016;305:537-561.
- 58. Kruggel-Emden H, Rickelt S, Wirtz S, Scherer V. A study on the validity of the multi-sphere discrete element method. *Powder Technol*. 2008;188(2):153-165.

- 59. Halphen B, Nguyen QS. Sur les matériaux standard généralisés. J de mécanique. 1975;14:39-63.
- 60. H Ziegler. An Introduction to Thermomechanics. Netherlands: North-Holland Publishing Company: 1977.
- 61. Arroyo M, Ortiz M. Local maximum-entropy approximation schemes: a seamless bridge between finite elements and meshfree methods. *Int J Numer Methods Eng.* 2006;65(13):2167-2202.
- 62. Li B. The optimal transportation method in solid mechanics [PhD thesis]. California Institute of Technology; 2009.
- 63. Parshikov AN, Medin SA, Loukashenko II, Milekhin VA. Improvements in SPH method by means of interparticle contact algorithm and analysis of perforation tests at moderate projectile velocities. *Int J Impact Eng.* 2000;24(8):779-796.
- 64. Lew A, Radovitzky R, Ortiz M. An artificial-viscosity method for the Lagrangian analysis of shocks in solids with strength on unstructured, arbitrary-order tetrahedral meshes. *J Comput-Aid Mater Des.* 2001;8(2-3):213-231.
- 65. Belytschko T, Liu WK, Moran B. Nonlinear Finite Elements for Continua and Structures. Hoboken, NJ: John Wiley & Sons; 2000.
- 66. Cuitino A, Ortiz M. A material-independent method for extending stress update algorithms from small-strain plasticity to finite plasticity with multiplicative kinematics. *Eng Comput.* 1992;9:437-437.
- 67. Lee EH. Elastic-plastic deformation at finite strains. J Appl Mech. 1969;36(1):1-6.
- 68. Simo JC, Miehe C. Associative coupled thermoplasticity at finite strains: formulation, numerical analysis and implementation. *Comput Methods Appl Mech Eng.* 1992;98(1):41-104.
- 69. Bonacina C, Comini G, Fasano A, Primicerio M. Numerical solution of phase-change problems. *Int J Heat Mass Transf*. 1973;16(10):1825-1832.
- 70. Radovitzky R, Ortiz M. Lagrangian finite element analysis of Newtonian fluid flows. Int J Numer Methods Eng. 1998;43(4):607-619.
- 71. Anisimov SI, Khokhlov VA. Instabilities in Laser-Matter Interaction. Boca Raton, FL: CRC Press; 1995.
- 72. Brackbill JU, Kothe DB, Zemach C. A continuum method for modeling surface tension. J Comput Phys. 1992;100(2):335-354.
- 73. Dong C-s, Wang G-z. Curvatures estimation on triangular mesh. J Zhejiang Univ Sci A. 2005;6(1):128-136.
- 74. Fukuhara M, Sanpei A. Elastic moduli and internal frictions of inconel 718 and ti-6al-4v as a function of temperature. *J Mater Sci Lett.* 1993;12(14):1122-1124.
- 75. Wunderlich RK. Surface tension and viscosity of industrial ti-alloys measured by the oscillating drop method on board parabolic flights. *High Temp Mater Process.* 2008;27(6):401-412.
- 76. Milošević N, Aleksić I. Thermophysical properties of solid phase ti-6al-4v alloy over a wide temperature range. *Int J Mater Res.* 2012;103(6):707-714.
- 77. Aboulkhair NT, Simonelli M, Parry L, Ashcroft I, Tuck C, Hague R. 3d printing of aluminium alloys: additive manufacturing of aluminium alloys using selective laser melting. *Prog Mater Sci.* 2019;106:100578.
- 78. Tallon JL, Wolfenden A. Temperature dependence of the elastic constants of aluminum. J Phys Chem Solids. 1979;40(11):831-837.
- 79. Assael MJ, Kakosimos K, Michael Banish R, et al. Reference data for the density and viscosity of liquid aluminum and liquid iron. *J Phys Chem Ref Data*. 2006;35(1):285-300.
- 80. Powell RW, Ho CY, Liley PE. *Thermal Conductivity of Selected Materials*. Vol 8. Washington, DC: US Department of Commerce National Bureau of Standards; 1966.
- 81. Buyco EH, Davis FE. Specific heat of aluminum from zero to its melting temperature and beyond equation for representation of the specific heat of solids. *J Chem Eng Data*. 1970;15(4):518-523.
- 82. Bainbridge IF, Taylor JA. The surface tension of pure aluminum and aluminum alloys. Metall Mater Trans A. 2013;44(8):3901-3909.
- 83. Zhang J, Song B, Zhang L, Liu J, Shi Y. Selective laser melting of al6061 alloy: processing, microstructure, and mechanical properties. Paper presented at: Proceedings of the 29th Annual International Solid Freeform Fabrication Symposium, Austin, Texas, USA; 2018:1253-1261.

How to cite this article: Fan Z, Wang H, Huang Z, et al. A Lagrangian meshfree mesoscale simulation of powder bed fusion additive manufacturing of metals. *Int J Numer Methods Eng.* 2020;1–32. https://doi.org/10.1002/nme.6546

APPENDIX

The fully discrete mechanical and thermal balance equations are

$$\mathbf{f}_{a,n+1}^{int} - \mathbf{f}_{a,n+1}^{ext} = m_{a,n+1}\ddot{\boldsymbol{\varphi}}_{a,n+1},$$
 (A1)

$$Q_{a,n+1}^{int} - Q_{a,n+1}^{ext} = 0, (A2)$$

where

$$m_{a,n+1} = \sum_{\mathbf{x}_{p,n} \in N_H(\mathbf{x}_{a,n})} m_p N_a(\mathbf{x}_{p,n}),$$
 (A3)

is the lumped mass of a node x_a interpolated from the mass of material points in its support $N_H(x_{a,n})$, and

$$\ddot{\boldsymbol{\varphi}}_{a,n+1} = \frac{2}{t_{n+1} - t_{n-1}} \left(\frac{\boldsymbol{x}_{a,n+1} - \boldsymbol{x}_{a,n}}{t_{n+1} - t_n} - \frac{\boldsymbol{x}_{a,n} - \boldsymbol{x}_{a,n-1}}{t_n - t_{n-1}} \right),\tag{A4}$$

is the nodal acceleration approximated using a central difference scheme. The internal nodal mechanical force $\mathbf{f}_{a,n+1}^{int}$ is described as

$$\mathbf{f}_{a,n+1}^{int} = \sum_{p \in N_H(\mathbf{x}_{a,n})} [\mathbf{P}^e(\mathbf{F}_{p,n+1}) + \mathbf{P}^v(\dot{\mathbf{F}}_{p,n+1})] \cdot \nabla N_a(\mathbf{x}_{p,n}) v_{p,n},$$
(A5)

and the external nodal mechanical force $f_{a,n+1}^{ext}$ follows

$$\mathbf{f}_{a,n+1}^{ext} = \sum_{p \in N_H(\mathbf{x}_{a,p})} \rho_{p,n} \mathbf{B}_{p,n+1} N_a(\mathbf{x}_{p,n}) \nu_{p,n} + \sum_{q \in \Gamma_t(\mathbf{x}_{a,p})} \overline{\mathbf{T}}_{q,n+1} N_a(\mathbf{x}_{q,n}) A_{q,n}, \tag{A6}$$

where v_p and A_q are the material point volume and surface area associated with a surface integration point, respectively. The internal and external nodal thermal forces for temperature evolution are given by

$$Q_{a,n+1}^{int} = \sum_{p \in N_{H}(\mathbf{x}_{a,n})} \nu_{p,n} \left\{ (\eta_{p,n} - \eta_{p,n+1}) N_{a}(\mathbf{x}_{p,n}) + [\mathbf{P}^{v}(\dot{\mathbf{F}}_{p,n+1}) : \Delta \mathbf{F}_{p,n} + \mathbf{Y}^{d}(\dot{\mathbf{Z}}_{p,n+1}) \cdot \Delta \mathbf{Z}_{p,n}] \frac{N_{a}(\mathbf{x}_{p,n})}{T_{p,n}} + \frac{\Delta t}{T_{p,n+1}} \mathbf{q}(T_{p,n+1}) \cdot [\nabla N_{a}(\mathbf{x}_{p,n}) + \mathbf{G}_{p,n+1} N_{a}(\mathbf{x}_{p,n})] \right\},$$
(A7)

and

$$Q_{a,n+1}^{ext} = \sum_{q \in \Gamma_a(\mathbf{x}_{q,n})} \Delta t \overline{h}_{q,n+1} \frac{N_a(\mathbf{x}_{q,n})}{T_{q,n+1}} A_{q,n} - \sum_{p \in N_B(\mathbf{x}_{q,n})} \Delta t \rho_{p,n} Q_{p,n+1} \frac{N_a(\mathbf{x}_{p,n})}{T_{p,n+1}} \nu_{p,n}, \tag{A8}$$

respectively.